UNIVERSITATEA “BABEȘ-BOLYAI” CLUJ-NAPOCA

FACULTATEA DE FIZICĂ

SPECIALIZAREA BIOFIZICĂ ȘI FIZICĂ MEDICALĂ

LUCRARE DE DISERTAȚIE

Coordonator Științific

Conf. Dr. Monica Focșan

Absolvent

Vlad Gabriel Cucuiet

2025

UNIVERSITATEA “BABEȘ-BOLYAI” CLUJ-NAPOCA

FACULTATEA DE FIZICĂ

SPECIALIZAREA BIOFIZICĂ ȘI FIZICĂ MEDICALĂ

LUCRARE DE DISERTAȚIE

Probing the Local Field Enhancement on Graphene-Plasmonic nanoplatforms Using DNA Strands of Varying Length and Grafting methods

Coordonator Științific

Conf. Dr. Monica Focșan

Absolvent

Vlad Gabriel Cucuiet

2025

Abstract

This dissertation presents a rigorous investigation into the capabilities of Surface-enhanced Raman Spectroscopy (SERS), a highly sensitive analytical technique, for the detailed analysis of nucleic acids. This research aimed to systematically understand how the SERS signal of a polyAdenine (polyA) strand is affected by two critical factors: its physical length(5, 10, 15 and 20 bases) and the specific chemical method used to attach it to a sensing surface. To achieve this, we employed a nanoplatform consisting of gold nanoparticles (AuNPs) synthesized directly onto graphene oxide (GO) sheets (denoted further as GO-AuNPs).

In this matter, firstly I synthesize the GO using the Hummers protocol [1]. The AuNPs were synthesized *in situ, by* reducing the gold ions directly onto the GO surface [2]. To confirm the successful of the synthesis, I conducted UV-VIS measurements. In addition, the morphology of the nanoplatform was investigated using Scanning Electron Microscopy.

On this GO-AuNP surface, we grafted polyA strands using four different lengths, containing 5, 10, 15, and 20 adenine bases, respectively and with two different 5' ending, SH and NH_2. Furthermore, we compared two distinct grafting strategies: attaching the polyA(SH at 5' end) at the surface of the AuNPs and the polyA(NH_2 at 5' end) to the functional groups of GO. Then, I conducted SERS measurements for all the designed configurations.

Our key finding was a strong and consistent correlation between the length of the DNA strand and the intensity of the characteristic adenine peak observed at 732 cm^{-1} in the SERS spectrum. This correlation was better for the system with polyA(NH_2 at 5' end) due to its strategic position in regions with high field enhancement called *hot-spots* between coupled gold nanoparticles. To understand the underlying mechanism, I performed Finite Difference Time Domain numerical simulations which confirmed that these intensity variations are governed by the positioning of the DNA strands in different regions with different electromagnetic fields amplification. Our experimental results allow us to effectively probe the strength and spatial decay of these localized electromagnetic fields, providing fundamental insights for designing future SERS-based biosensors.

Table of Contents

Introduction

The rapid advancement of nanotechnology and spectroscopy has catalyzed considerable progress in the development of sensitive biosensing platforms. Among these, DNA biosensing has emerged as a critical field, offering profound implications for early disease detection, environmental monitoring, and personalized medicine. The ability to detect and analyze nucleic acids with high sensitivity and specificity is essential for applications ranging from clinical diagnostics to forensic science.

At the heart of this innovation is Surface Enhanced Raman Spectroscopy (SERS), a powerful analytical tool capable of amplifying Raman scattering signals from molecules adsorbed on nanostructured metallic surfaces. SERS exploits the electromagnetic field enhancement that occurs at the surface of plasmonic materials, such as gold and silver nanoparticles. This enhancement can be of several orders of magnitude higher than the intrinsic Raman signal, enabling the detection of molecular species at extremely low concentrations [3], [4], [5]. The phenomenon is primarily governed by the local electromagnetic fields generated near these nanostructures, which makes the study of local field distributions critically important for the rational design of high-performance sensors.

Local field probing is an essential aspect of understanding and optimizing plasmonic biosensors. By mapping the electromagnetic field intensity around nanostructured surfaces, researchers can gain insights into how different configurations, materials, and molecular interactions influence the sensor's performance. This local field effect is particularly significant in the context of DNA biosensing, where the precise spatial arrangement and orientation of DNA strands relative to plasmonic *hot-spots* can dramatically affect the sensitivity and specificity of detection. Therefore, exploring the interplay between nanostructure-induced field enhancements and biomolecular recognition processes is a key challenge in the field.

Recent advances in materials science have provided new avenues for constructing hybrid nanoplatforms that combine the unique properties of two-dimensional materials with those of metal nanoparticles. For instance, graphene oxide (GO) has attracted considerable attention due to its excellent chemical, mechanical, optical properties and due to its capability to enhance the absorbance of the molecules [6], [7], [8], [9].

Graphene materials and gold nanoparticles (AuNPs) form a highly synergistic hybrid system that enhances the performance of biosensors, particularly in plasmonic applications such as SERS. Graphene, a two-dimensional material composed of sp^2-hybridized carbon atoms, provides a large surface area, excellent electrical conductivity, and chemical stability, making it an ideal platform for anchoring AuNPs [6], [7], [9]. The interaction between graphene/graphene oxide and AuNPs occurs primarily through electrostatic forces, and van der Waals interactions, which facilitate the uniform dispersion of nanoparticles onto the graphene/graphene oxide surface [7], [10], [11]. Additionally, graphene/graphene oxide helps stabilize AuNPs, preventing aggregation and ensuring reproducibility in biosensing applications [8]. Moreover, regarding the signal enhancement it is known that different graphene materials can contribute to SERS signal through Chemical Enhancement, more specifically due to electron Charge Transfer to the molecule of interest [3], [12], [13], [14], [15]. In this context, integration of graphene-related materials and metal nanoparticles can enhance the actual biosensing limitations by improving the stability and limit of detection of the sensors.

To observe the high interest in integrating graphene materials with SERS across different research area, I plot in Figure I.1 a PieChart of WebOfScience categories resulting after “graphene based SERS” search. As we can see, the domain is strongly interdisciplinary, and the graphene-metal nanoparticles nanostructures are used in different areas.

The synergistic combination of graphene materials and gold nanoparticles enhances molecular adsorption, facilitates charge transfer, and enables easy functionalization, making it highly beneficial for developing sensitive SERS biosensors. This integration not only improves detection sensitivity but also provides robust stability and tunable optical properties, paving the way for the design of multifunctional biosensors with enhanced performance.

DNA molecules, owing to their intrinsic specificity and programmability, represent ideal candidates for molecular recognition in biosensing applications. The integration of DNA with plasmonic nanomaterials facilitates the development of sensors that are both selective and highly responsive [16], [17], [18], [19], [20]. The DNA strands can be used to serve as recognition elements, linking the binding of target molecules to measurable changes in the local electromagnetic environment. Consequently, monitoring these changes through

SERS provides a direct route to detecting and quantifying biomolecular interactions at the nanoscale.

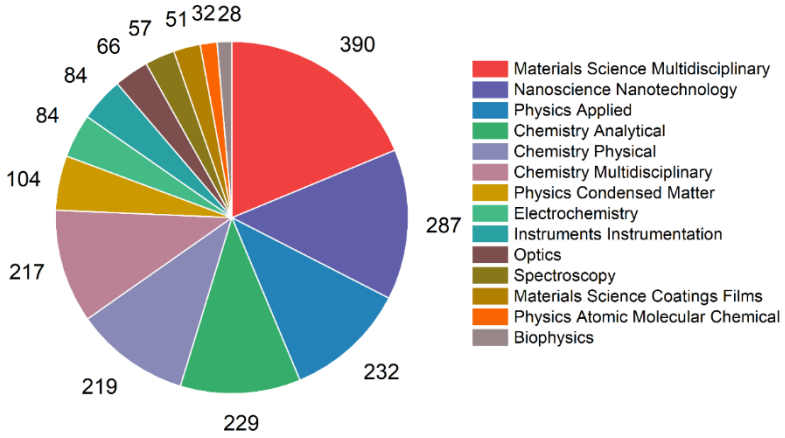

Figure I.1. PieChart of WebOfSCience categories of "graphene based SERS" search.

The convergence of DNA biosensing and local field probing represents a fertile ground for both fundamental research and technological innovation. By leveraging advanced spectroscopic techniques alongside state-of-the-art nanomaterial synthesis, researchers can gain a deeper understanding of the mechanisms that govern plasmonic enhancements. This, in turn, paves the way for the development of next-generation diagnostic tools that are not only extremely sensitive but also capable of providing detailed molecular information.

In this study, we probe the electromagnetic field enhancement using the detection of DNA grafted onto graphene oxide-gold nanoparticles (GO-AuNPs) nanoplatforms. Specifically, we utilized polyA strands of varying lengths (5, 10, 15, and 20 bases) with two distinct 5' end terminations: thiol (SH) and amine (NH_2). Using both types of DNA, I strategically placed the polyA strand in two different locations:

1. The polyA(SH at 5' end) is bonded directly to the AuNP through a covalent thiol bond.
2. The polyA(NH_2 at 5' end) is bonded onto the graphene oxide layer through a covalent amine bond. Here, the strand is placed between coupled AuNPs.

Therefore, using different lengths of ssDNA strands, we probe the local field enhancement generated by isolated AuNPs and by coupled AuNPs in different locations, therefore finding the profile of the generated electromagnetic field enhancement. Also, I validate this model using Finite Difference Time Domain (FDTD) simulations.

FDTD simulations are a computational technique widely used to model and analyze the behavior of electromagnetic fields over time. This method breaks down Maxwell's equations, which govern electromagnetic interactions, into discrete time and space intervals, allowing the simulation to compute how fields evolve over both dimensions. By dividing the simulation space into a fine grid and advancing the field values in small time and size steps, FDTD can capture the complex interactions between electromagnetic waves and various materials. This level of detail makes it especially valuable for simulating nanostructures, plasmonic materials, and photonic devices where conventional analytical methods struggle to provide accurate predictions due to the intricacy of these interactions. In practical applications, FDTD is used in the design and analysis of optical devices, antennas, sensors, and plasmonic nanostructures. It is instrumental in predicting field enhancements near nanoparticles or structures designed for SERS. Despite its computational intensity, advances in processing power have made FDTD a powerful tool in modern computational electromagnetics, providing accurate, high-resolution insights into field distributions and device performance [21], [22], [23].

This thesis is divided into two main chapters, one with theoretical explanations and one with the experimental results obtained during my master's degree.

Chapter 1 contains theoretical aspects of Raman spectroscopy and SERS explaining the enhancement mechanism of SERS, the electromagnetic and chemical enhancement, respectively. Also, in this chapter I detailed aspects about the integrating of graphene into SERS spectroscopy with applications in DNA biosensing.

In **Chapter II** I presented the experimental results and theoretical simulations of this study are presented. In summary, I started by synthesizing GO using an improved Hummers protocol. I characterized the GO using UV-VIS spectroscopy and Scanning Electron Microscopy (SEM). Then, I synthesized the GO-AuNPs colloidal solution using a modified Turchevik synthesis. Here, the AuNPs are directly synthesized onto the GO sheets being bond electrostatically to GO. The next step was to bond the two DNAs strand to the GO-AuNPs nanoplatforms. For the first one, I attached the polyA(SH at 5' end) to the AuNP surface through a thiol bons, and for the second nanoplatform I attached the polyA(NH_2 at 5' end) to GO via an amine bond using the EDC protocol. In both cases, I used four different polyA strands with different numbers of bases (20, 15, 10 and 5 bases). Afterwards, I characterize both nanoplatforms using UV-VIS Spectroscopy, Scanning Electron

Microscopy (SEM), Energy Dispersive X-Ray (EDX) and Raman Spectroscopy. I conducted FDTD simulation to calculate the field enhancement of isolated AuNP and of coupled AuNPs to prove the model proposed. Using these results, I was able to probe the field enhancement as a function of distance using polyA strands with different grafting methods and lengths.

The results obtained in this thesis were published in the following article [24] : "Probing the Local Field Enhancement Using SERS Detection of DNA Strands with Different Lengths and Grafting Strategies on Graphene Oxide Plasmonic Nanoplatforms": **Vlad Cucuiet**, Dana Maniu, Ana Maria Craciun, Septimiu Tripon, Simion Aștilean, Marc Lamy de la Chapelle, Monica Focsan, J. Phys. Chem. Lett. 2025, 16, 2, 435–442 (IF 4.6, Nature Index). Also, the article was selected for the cover art for its respective issue (right image).

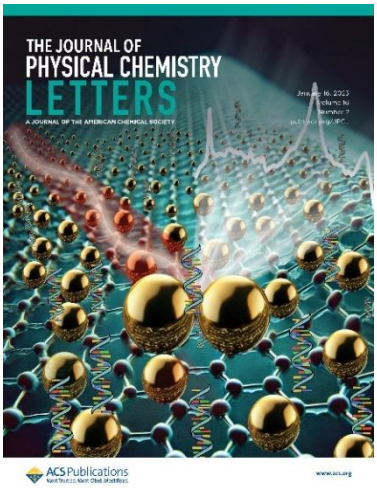

During my master studies, I also published two review articles, from which one as a principal author:

1. **Vlad Cucuiet**, Dana Maniu, Simion Astilean, Marc Lamy de la Chapelle, Monica Focsan; Graphene-mediated surface enhanced Raman spectroscopy for DNA Detection&hybridization: Breakthroughs and challenges. Elsevier, Biosensors and Bioelectronics, 2025, 286, 117610 (IF 10.5). [25].
2. Alexandru Holca, **Vlad Cucuiet**, Simion Astilean, Marc Lamy de la Chapelle, Monica Focsan; Recent advances in gold nanoparticle-graphene hybrid nanoplatforms with visible to near-infrared response for photodynamic and photothermal therapy and bioimaging, RSC Adv, 2025, 15,11902-11922 (IF 4.6). [26]

In this thesis I used with permission different figures and parts of text from the articles mentioned above.

Also, these results were presented at the International Conference on Raman Spectroscopy 28 July-2 August 2024, Rome, Italy.

1. **Vlad Cucuiet**, Monica Potara, Marc Lamy de la Chapelle, Simion Astilean, Monica Focsan; Graphene mediated SERS detection of DNA hybridization. ICORS XXVIII, 2024, Rome, Italy.

Chapter 1.Theoretical Aspects

1.1.What is Surface Enhanced Raman Spectroscopy?

Raman spectroscopy is one of the most widely used analytical techniques in vibrational spectroscopy today, providing essential information about the vibrational modes of the analyzed chemical compounds. Raman spectroscopy is based on the Raman effect [27], [28]. The Raman effect, when talking about molecules, describes the inelastic scattering process between a photon and a molecule. This process is mediated by a fundamental vibrational mode of the molecule. Due to this mediation, energy exchange occurs between the photon and the molecule, and the photon energy is shifted by the characteristic energy of the molecule's vibration. The shifts can be both positive and negative with reference to the incoming electromagnetic radiation energy, depending on if the molecule is found in the ground or excited state. If the molecule is in the ground state, the photon loses energy by excitation of a vibrational mode (Stokes scattering) and in the second case, the photon gains energy due to the vibrational de-excitation of the molecule (anti-Stokes scattering). (Figure 1.1).

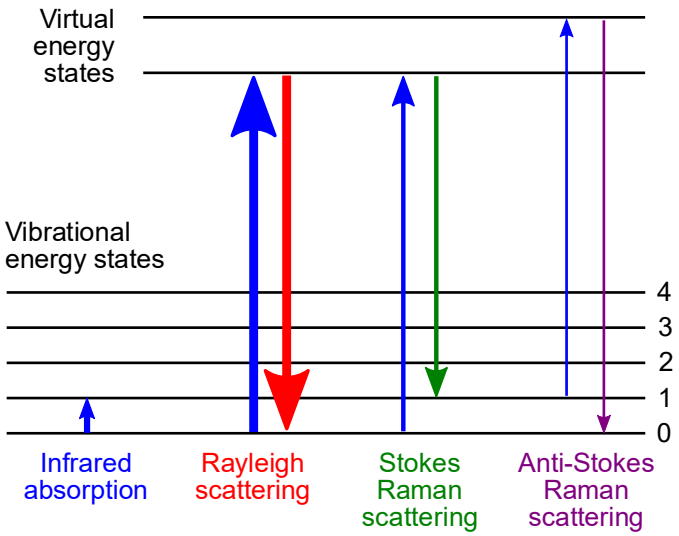

Figure 1.1. Vibrational Transition of electrons in Raman Effect. Image taken from [29]

The total power of the scattered light due to the Stokes scattering process can be written as:

$$P_S(\nu_S) = N\,\sigma_{RS}\,I(\nu_L),$$

Where N is the number of excited molecules, σ_{RS} is the scattering cross-section, and $I(\nu_L)$ is the intensity of the excitation beam. Therefore, to be able to measure low-concentration solutions (thus decreasing N), we need a technique to increase the total power of the scattered light. One of the most used techniques is called Surface Enhanced Raman Spectroscopy (SERS).

SERS is an advanced spectroscopic technique that significantly enhances the weak Raman scattering signals of molecules, making it a valuable tool for highly sensitive chemical and biochemical analysis. SERS effect was first observed in 1974 by M. Fleischmann at University of Southampton who reported a high-intensity spectra of pyridine adsorbed on a silver electrode[30]. In 1977, R.P. Van Duyne and D.L. Jeanmaire from Northwestern University reproduced the experiment and calculated that the Raman cross-section of the pyridine adsorbed on the silver electrode increase by a factor of 10^5-10^{-6} [31].

This enhancement occurs when molecules are absorbed onto nanostructured metallic surfaces, such as gold, silver, or copper, which are known for their plasmonic properties. SERS relies on two primary mechanisms: **electromagnetic enhancement** and **chemical enhancement**, which work together to amplify the Raman signal by 7-8 orders of magnitude [4]. In case of SERS, the increase of the P_S is due to two effects.

A. **Increasing the scattering cross-section of the molecule, process known as Chemical Enhancement:** This mechanism arises from the interaction between the adsorbed molecule and the metal surface or another molecule, often through charge transfer processes (Figure 1.2c). When a molecule adsorbs onto the metallic surface, it can form a chemical bond or undergo electronic coupling with the surface, altering its electronic structure [32], [33], [34], [35], [36]. This interaction increases the polarizability of the molecule, making it more responsive to the oscillating electric field of the incident light and enhancing the Raman signal. Moreover, by changing the electronic structure of the molecule, the electronic transition can become resonant with the laser energy, therefore increasing the signal. Chemical enhancement is highly molecule-specific, influenced by the nature of the adsorbed species and the surface chemistry of the substrate.
B. **Electromagnetic enhancement**, the dominant mechanism, is driven by the excitation of localized surface plasmon resonances (LSPRs) in the metallic nanostructures and the accumulation of the electric field lines at the metal interfaces (lightning rod effect). This phenomenon arises when the frequency of the incident electromagnetic field

matches the natural frequency of the electron oscillations (Figure 1.2a), leading to a resonant enhancement of the local electromagnetic field around the nanoparticles [3], [37], [38]. These fields are particularly intense in regions known as *hot-spots* often found at sharp edges, tips, or junctions between nanoparticles (Figure 1.2b). This leads to the enhancement of both the incident and scattered light. The enhancement factor can be written as $L(\nu) = |E_{loc}(\nu)|/|E_0|$, which is the ration between the field due to the SERS effect and the field of Raman Scattering. Therefore, the new total power of the Stokes beam due to SERS effect is [39]:

$$P_S(\nu_S) = N\ \sigma_{SERS} L(\nu_L)^2 L(\nu_S)^2\ \ I(\nu_L),$$

Since the $|\ L(\nu_L)| \sim |\ L(\nu_S)|$, the electromagnetic contribution to the total SERS enhancement is proportional to the 4^{th} power of the field enhancement factor. Therefore, we can write the enhancement factor of the Stokes beam as follows [40]:

$$R = \frac{|E_{loc}|^4}{|E_0|^4}$$

Molecules located in these hot spots experience an amplified electric field, which boosts the intensity of both the incident laser light and the scattered Raman signal, leading to significant enhancement. The magnitude of this effect depends on the material, shape, size, and arrangement of the nanostructures, as well as the wavelength of the incident light.

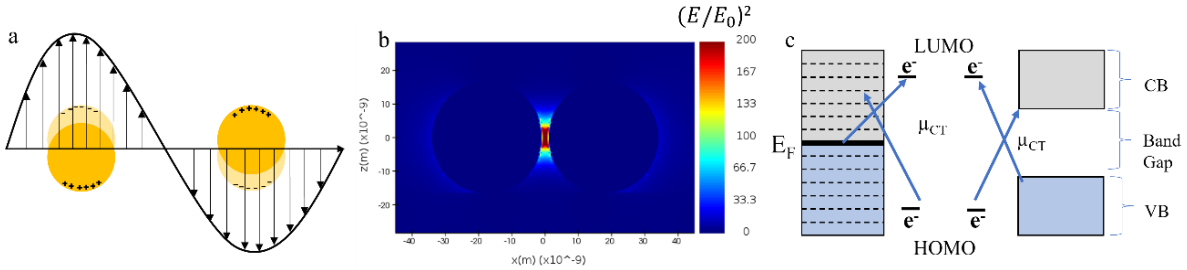

Figure 1.2. (a) Coherent oscillations of conductions electrons in metallic nanoparticles creating localized electromagnetic fields; (b) Coupled Nanoparticles generating high intensity electromagnetic field between them (*hot-spot*); Reprinted with permission from J. Phys. Chem. Lett. 2025, 16, 2, 435–442. Copyright 2025 American Chemical Society [24]; (c) Chemical Enhancement mechanism of SERS. Reprinted with permission from [25].

Together, these mechanisms enable SERS to achieve unprecedented sensitivity, capable of detecting single molecules under optimal conditions. This makes SERS an indispensable tool in fields such as chemical sensing, biological diagnostics, environmental monitoring, and materials science, where trace-level detection is often required. By carefully designing and optimizing the nanostructured substrates, researchers can harness the synergistic effects of electromagnetic and chemical enhancement to tailor SERS for a wide range of applications.

1.2. Using Graphene mediated Surface Enhanced Raman Spectroscopy in DNA Biosensing

SERS has emerged as a transformative tool in biosensing due to its exceptional sensitivity and molecular specificity, making it ideal for detecting and characterizing biological molecules [41]. Among its numerous applications, the detection of DNA stands out as a critical area, especially for identifying genetic mutations, monitoring diseases, and advancing personalized medicine [42], [43], [44]. DNA detection using SERS leverages the technique's ability to amplify weak Raman signals from DNA molecules, enabling the identification of specific nucleotide sequences even at extremely low concentrations. This capability is particularly important in scenarios such as early disease diagnosis, where biomarkers are present at trace levels in biological fluids. Traditional methods like polymerase chain reaction (PCR) are effective but often require extensive sample preparation and amplification steps, whereas SERS offers a label-free or minimally labeled alternative that can provide direct molecular insights even without prior knowledge of the DNA composition [45], [46], [47], [48]. Moreover, the unique Raman fingerprints of the four nucleotide bases (adenine, guanine, cytosine, and thymine) allow detailed structural analysis and sequence verification.

Also, in genetic analysis, the studies are practically applied to the central theme of gene mutations, specifically those characterized by DNA nucleobase mismatches. This phenomenon involves alterations in a gene's nucleotide sequence, including substitutions, insertions, or deletions of nucleobases [49], [50]. Using SERS and DNA detection and DNA-DNA hybridization, these mutations can be experimentally highlighted due to their pivotal role in influencing gene function and contributing to genetic diversity and disease development. For instance, SERS is preferred for detecting trace levels of biomarkers in the early stages of cancer because of its ultrasensitive and non-invasive nature [51]. Beyond

detection, classifying these gene mutations is a promising step toward differentiating various cancer types [52], [25].

Graphene can directly contribute to Raman signal enhancement, through a chemical mechanism involving charge transfer between graphene and the analyte molecules, facilitated by π–π interactions [53], [54]. Further enhancement of signal strength can be achieved by modifying graphene sheets through doping (e.g., with nitrogen) or mild reduction, which effectively reduces the energy difference between the molecule's highest occupied molecular orbital (HOMO) and graphene's Fermi level [54], [55], [25]. Graphene's exceptionally high thermal conductivity is another significant advantage. For example, suspended graphene exhibits thermal conductivities ranging from 1500 W/(m*K), while when oxidized, the GO can reach a thermal conductivity of around 1500 W/(m*K), depending on the degree of oxidation. These remarkable high conductivities enable efficient heat dissipation, which is critical for minimizing the risk of molecular degradation during laser irradiation when measuring SERS signals. Furthermore, graphene/graphene oxide has a negatively charged surface which makes them easy to functionalize with various molecules [56], [57], [58], [25].

Graphene-enhanced Raman Spectroscopy (G-SERS) represents a significant advancement in analytical techniques, utilizing graphene's distinctive properties to improve the sensitivity and precision of traditional Raman spectroscopy. The integration of graphene into the SERS methodology has established G-SERS as a potent tool capable of detecting and characterizing molecules at exceptionally low, femtomolar concentrations. For G-SERS, graphene has multiple roles. From SERS perspective, different studies indicate that G-SERS often provides clearer vibrational spectra and more comprehensive chemical information compared to conventional SERS investigations [59], [60].

By combining nanotechnology, advanced surface chemistry, and high-resolution spectroscopic techniques, SERS has revolutionized biosensing, offering a powerful platform for rapid, precise, and ultrasensitive DNA analysis in clinical and research settings [61], [62], [63], [64], [65], [66].

Chapter 2. Techniques and Experimental Results

2.1 Materials

Graphite flakes, 325 mesh size, 99.9995 % were purchased from Alfa Aesar (Germany). Sulfuric acid (H_2SO_4, 99%) and hydrogen peroxide (H_2O_2, 30%) were obtained from Nordic (Romania). The potassium permanganate ($KMnO_4$), Sodium Citrate, Natrium Chloride, 1-ethyl-3-(3- dimethylaminopropyl) carbo diimide hydrochloride (EDC), Gold (III) Chloride Trihydrate 99.9% were all purchased from Sigma-Aldrich. All polyA strands (SH or NH_2 at 5' end) with different number of bases (5, 10, 15 and 20 bases), RP-HPLC purified, were purchased from Eurogentec, Belgium. All the polyA was dissolved in TE buffer purchased from ThermoScietific and stored in the freezer. During all the experiments the ultrapure-water (resistivity ~18.2 MΩ) was obtained from the Milli-Q (Millipore, Merck, Massachusetts, USA) purification system.

2.2. Experimental Equipment

UV-VIS measurements were done using a Jasco V-670 UV-VIS-NIR spectrophotometer having a spectral resolution of 1 nm. All samples were measured in the range 190-900 nm at room temperature.

The morphology of the naonsystems were analyzed by Field-Emission Scanning Electron Microscopy (FE-SEM) using a Zeiss GeminiSEM 560. For the Energy Dispersive X-Ray (EDX) analysis we used the Oxford Ultim Max 100 mm detector at 20 kV. The samples were dropped onto a Silica substrate.

The SERS measurements were made using a Confocal Raman Spectrometer from Renishaw with a spectral resolution of 1 cm^{-1}. All the spectra were acquired using the following parameters: 785 nm laser line, 1 second time of acquisition, 20 acquisitions per spectrum, 1200 lines/mm diffraction gratings. The spectra were recorded by a RenCam CCD detector 1024x256 pixels. The optical microscope used was a Leica research grade coupled with a 20x objective (NA 0.35, WD 2mm). The SERS spectra were collected from a dried drop on aluminum foil. For each measurement I recorded around 30 spectra. The spectra analysis and the Principal Component Analysis (PCA) were done using OriginLab 2024 software.

Theoretical Simulations. Theoretical simulations of the electromagnetic field intensity and distribution around individual and coupled gold nanoparticles were performed using the FDTD Lumerical software from Ansys (https://www.ansys.com /products/ optics /fdtd), which is based on the Finite-Difference Time-Domain (FDTD) method. The AuNPs were modeled as gold spheres (Au) with a diameter of 33 nm, positioned in air (n = 1) on a substrate with a refractive index of 1.5. A mesh size of 0.2 nm was employed, and perfectly matched layers (PMLs) were applied in all directions to absorb outgoing waves. The simulations calculated the electromagnetic field intensity and distribution at a wavelength of 785 nm for both a single AuNP and a pair of coupled AuNPs separated by a 2 nm gap. A total-field scattered-field (TFSF) source was used, propagating perpendicular to the AuNPs' plane and polarized parallel to the substrate. To analyze the electromagnetic response at 785 nm, a field monitor was placed perpendicular to the substrate, intersecting the center of the AuNPs.

2.3. Methods

2.3.1 *In situ* synthesis of gold nanospheres onto Graphene Oxide nanosheets

Graphene Oxide (GO) was produced using a modified Hummers Protocol [1], [67]. The entire protocol is at it follows.

Firstly, I mixed the graphite flakes with 0.9 g of KNO_3 and 33.8 mL of H_2SO_4 (98%) for 3 hours at room temperature. After the reaction took place I obtained KNO_3 - H2SO4-GIC (Graphite Intercalated Compound)[68], an intermediate compound in which molecules of H_2SO_4 and KNO_3 are intercalated between graphite layers. The mixture was done under continuous stirring. After this step I set the temperature of the mixture around 3-4 °C using a proper ice bath. Then I slowly add 4.5 g of $KMnO_4$ as a strong oxidizing agent. This reaction is exothermic; thus, the temperature can increase rapidly. Due to the reaction of $KMnO_4$ and H_2SO_4, the graphite starts to oxidize, the solution becoming green-ish.

The oxidation time depends on the size of the graphite flakes. For our 300 mesh size, we let the mixture react for about 2 days under continuous stirring until the color changes from green to brown and the viscosity of the solution increases. After the oxidation step is finished, I diluted the mixture with 110 mL H_2SO_4 (5% wt) solution and let the mixture to homogenize for 3 hours. The next step was to remove the unreacted $KMnO_4$ adding 3g of H_2O_2 (30%). This reaction is strongly effervescent. After another 3 hours, I further diluted

the solution with 100 mL of H_2SO_4 ($3wt\%$) and H_2O_2(0.5 wt%, 30%) solution and let it under stirring for another 3 hours (Figure 2.1a).

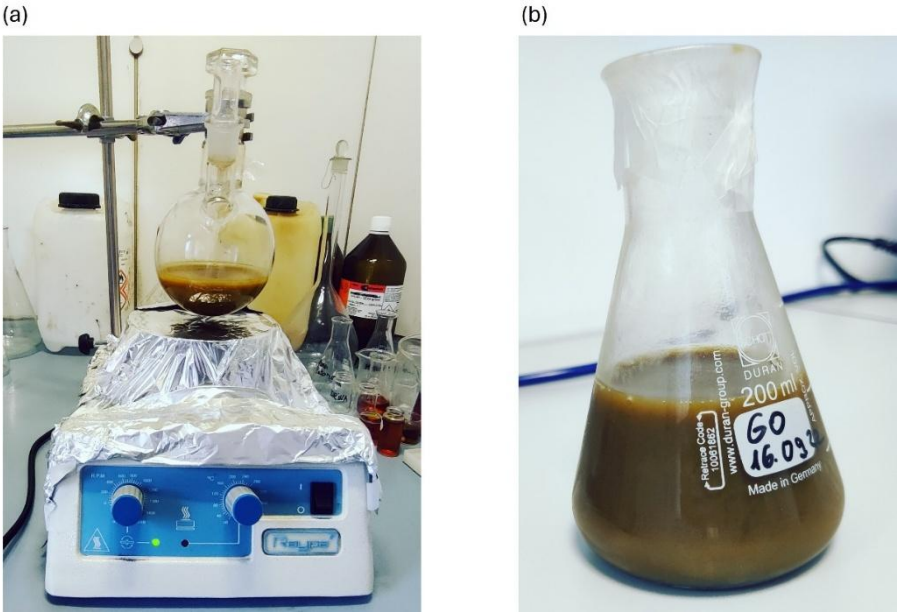

Figure 2.1. (a) Image of GO in H_2SO_4-H_2O_2 solution, (b) Image of final aqueous GO solution

The final solution is purified using multiple centrifugation (10-15) at 6000 RPM. For the first 6 centrifugations, the supernatant is eliminated and changed with a solution of 3wt% H_2SO_4 – 0.5wt% H_2O_2(30%). The solution is well-homogenized before each centrifugation. After this, for the next 6 centrifugations I used only ultrapure water. Initially, the centrifugation time is around 30 minutes. After a few centrifugations it is observed that the volume of the precipitate increases, becoming more soluble in water. Now, the centrifugation time must be increased gradually until reached 1.5 hours.

After the purification steps, the GO solution is collected and stored in fridge (Figure 2.1b).

The colloidal solution of Graphene Oxide Gold Nanoparticles (GO-AuNPs) was prepared through an *in situ* reaction. Here, $HAuCl_4$ was reduced in the presence of GO and sodium citrate, leading to the direct formation of AuNPs on the GO layers [2]. The AuNPs are bonded electrostatically to the GO sheets. Initially, 3 mg of sodium citrate was dissolved into 0.3 mL of water, and a 3 mL solution of GO (0.1 mg/mL) was prepared. Both solutions were added to 30 mL of ultrapure water, and the mixture was continuously stirred while heated to 90-95°C. Once the target temperature was reached, 400 µL of $HAuCl_4$ (25 mM) was rapidly introduced, and the solution was stirred for an additional 10 minutes while

maintaining the heat. During this step, the solution color changes from transparent to red-purple which proves the formation of AuNPs, as seen in Figure 2.2.

Figure 2.2. Image of a GO-AuNPs colloidal solution

Afterward the stirring continued until the solution cooled to room temperature. The final mixture was centrifuged at 9500 RPM for 25 minutes to remove the supernatant, and the resulting pellet was redispersed in water at the desired optical density. The final solution was stored in a refrigerator until further use.

2.3.2 Grafting of the polyA(SH and NH_2 at 5' end) onto GO-AuNPs nanoplatforms

For this study we used two grafting methods of the polyA to the GO-AuNPs nanoplatform. Firstly, we graft the polyA directly to the AuNPs via a thiol bond using a thiolate polyA with -SH terminal at 5' end (polyA(SH at 5' end)). For this grafting method we mix 10 µL of polyA(SH at 5' end) at 10^{-6} M concentration with 5 µL of tris(2-carboxyethyl)phosphine (TCEP) at 5 µM to break the disulfide bonds and let it sit for 2 hours at room temperature. Then I added 20 µL of GO-AuNPs colloidal solution and the mixture was kept at room temperature overnight. To decrease the repulsion between the polyA backbones, thus increasing polyA(SH at 5' end) density, 2 µL of NaCl was added 2-3 times at 1.5 hours interval.

For the second grafting method, we bond the polyA directly to the GO layer. For this case we utilized amino modified polyA strands (polyA(NH_2 at 5' end)). To graft the polyA(NH_2 at 5' end) to GO surface we create an amine bond between the polyA(NH_2 at 5' end) and GO functional groups. We mixed 10 µL of polyA (10^{-6} M), 5 µL of freshly prepared

1-ethyl-3-(3-dimethylaminopropyl)carbodiimide) (EDC) solution at 20 mM, 20 µL GO-AuNPs and 2 µL of NaCl (0.1 mM).

For both grafting methods, we utilized 5 different lengths of polyA strand: 5, 10, 15 and 20 bases, respectively. The synthesis protocols are the same regarding the number of the bases of the polyA strand.

As for the hybridization of the as fabricated GO-AuNPs-polyA nanoplatforms we used polyThymine (polyT) as complementary strand at different concentrations: 10^{-4}, 10^{-5}, 10^{-6} and 10^{-7} M. For each hybridization we matched the length of the polyT with the length of polyA strand.

2.4. Experimental Characterization and Results

2.4.1. UV-VIS and SEM images of GO, GO-AuNPs and GO-AuNPs-polyA

We first characterized our samples using Absorption Spectroscopy. Figure 2.3a represents the GO absorption spectra (Figure 2.3a, green line). Here, we clearly observe the two characteristic bands of GO, the one at 231 nm corresponding to π- π* transition and the shoulder at around 300 nm which is due to n- π* transition [6], [7]. The SEM image of GO can be seen in Figure 2.4a. In Figure 2.3a (red line) we observed the GO-AuNPs extinction spectrum. Here a new band at 532 nm appeared corresponding to the plasmonic band of the AuNPs. Also, due to the mild reduction of GO during the synthesis of GO-AuNPs, a broadening of the 231 nm band occurs [69], [70], [71]. The presence of the AuNPs on GO layer was proved using SEM (Figure 2.3a inset and Figure 2.4b) . The mean diameter of the AuNPs calculated from SEM images was 34 ± 7 nm.

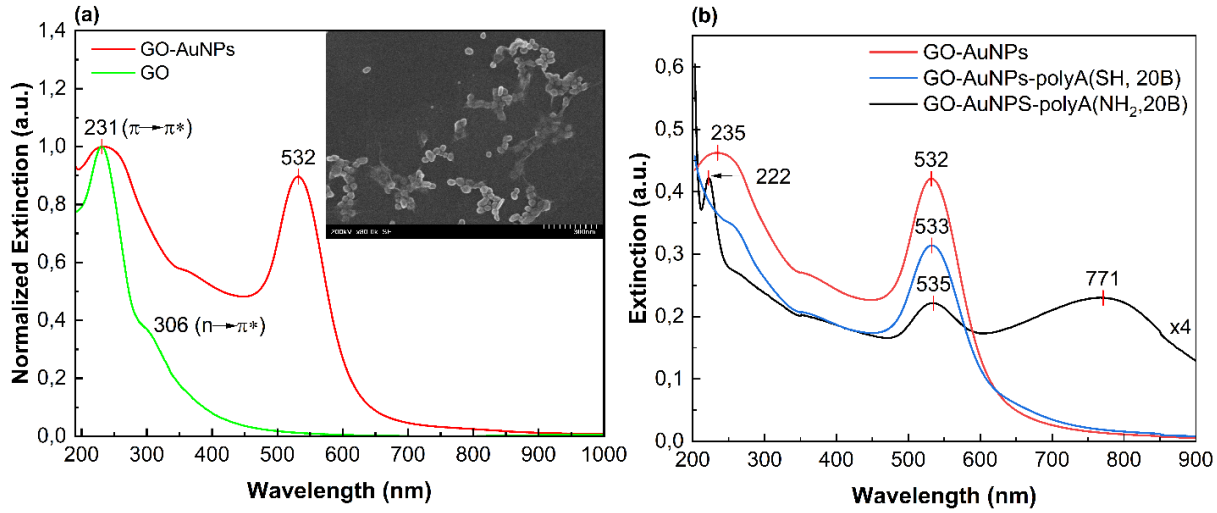

Figure 2.3. (a) UV-VIS spectra of GO (green line) and), GO-AuNPs (red line);) and inset the SEM image of GO-AuNPs; (b) - UV-VIS spectra of GO-AuNPs(red line), GO-AuNPs-polyA(SH 20B) (blue line) and GO-AuNPs-polyA(NH_2 20B) (black line); Reprinted with permission from J. Phys. Chem. Lett. 2025, 16, 2, 435–442. Copyright 2025 American Chemical Society [24].

The GO-AuNPs-polyA nanostructures were also characterized via UV-VIS Spectroscopy. For GO-AuNPs-polyA(SH at 5' end) we observed a shift of 1 nm in the plasmonic band as compared to the GO-AuNPs (Figure 2.3b, blue spectrum), thus confirming the covalent bond between the thiolate polyA and AuNPs. For the case of GO-AuNPs-polyA(NH_2 at 5' end) we observed a 3 nm blue shift and broadening of the main plasmonic band and a new sharp band at 222 nm appears which correspond to the EDC involved in the synthesis. Also, after the bonding of polyA(NH_2 20B) to the GO-AuNPs controlled aggregation of AuNPs is induced, generating a strong coupling effect between nanoparticles. Due to this coupling, a second plasmonic band appeared ad 771 nm which is attributed to aggregated AuNPs, the main plasmonic band at 535 nm being attributed to free spherical AuNPs[72], [73]. The morphology of the GO-AuNPs-polyA(NH_2 at 5' end) was further studied using Scanning Electronic Microscopy (SEM) shown in Figure 2.4c.

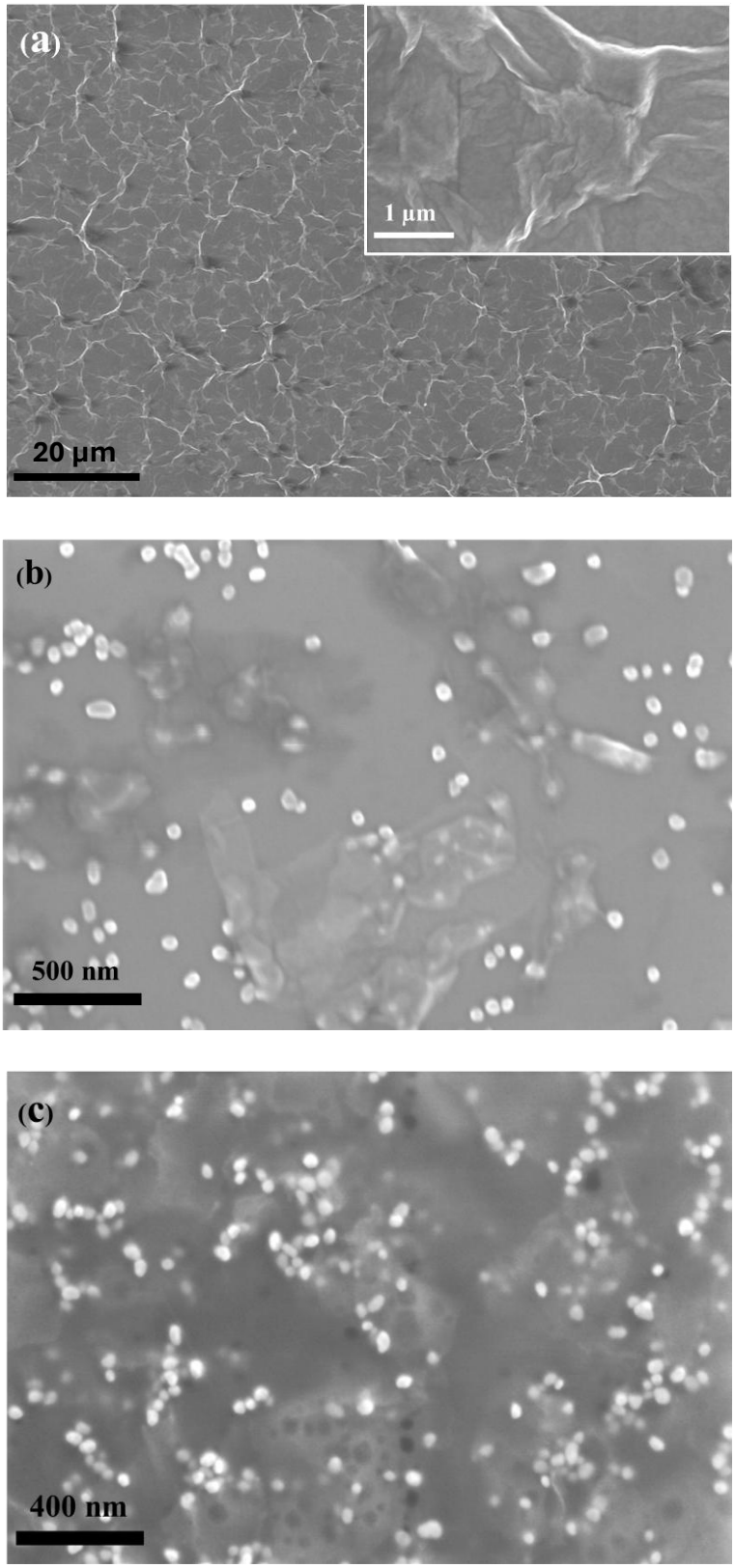

Figure 2.4. FE-SEM images of (a) GO, (b) GO-AuNPs and (c) GO-AuNPs-polyA(NH2 20B). Reprinted with permission from J. Phys. Chem. Lett. 2025, 16, 2, 435–442. Copyright 2025 American Chemical Society [24].

Also, to further prove the presence of the polyA(NH_2 at 5' end) strand in our system, we conducted Energy Dispersive X-ray (EDX) measurements. In Figure 2.5 are displayed the EDX histogram of the element composition alongside a table with the atomic ration of each element, for GO-AuNPs (Figure 2.5a) and GO-AuNPs-polyA(NH_2 at 5' end) (Figure 2.5b)

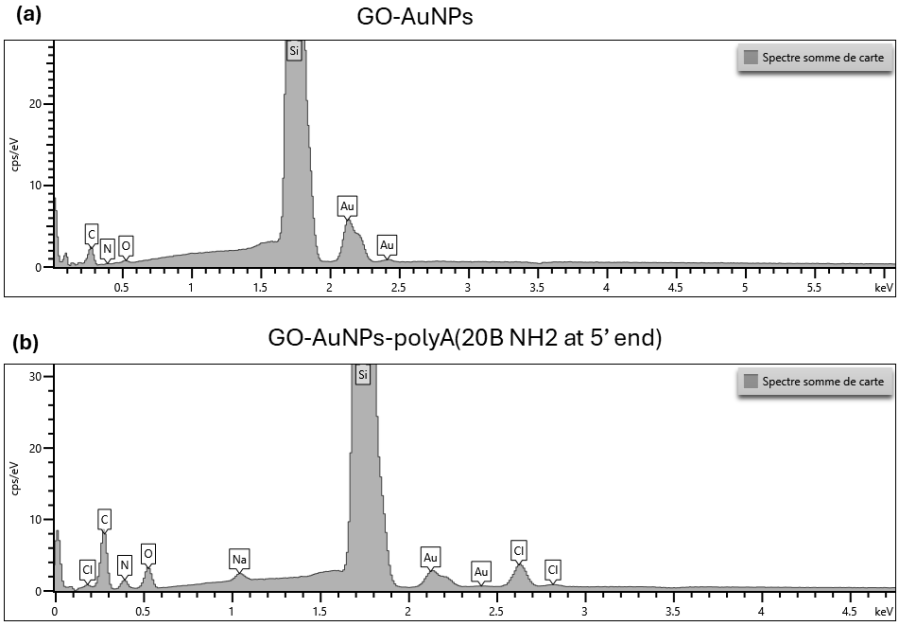

Element	% atomic
C	40.9
N	0.38
O	0.83
Si	57.89

Element	% atomic
C	55.9
N	8.76
O	5.07
Na	0.16
Si	29.64
Cl	0.47

Figure 2.5. EDX measurements on GO-AuNPs (a), and on GO-AuNPs-polyA(20B NH_2 at 5' end). On the right, the tables corresponding to the atomic mass percentage on each sample. Reprinted with permission from J. Phys. Chem. Lett. 2025, 16, 2, 435–442. Copyright 2025 American Chemical Society [24].

As can be seen from the tables from Figure 2.5, we have a significant increase in the atomic concentration of C, N and O atoms in GO-AuNPs-polyA(NH_2 at 5' end) (down table) as compared to GO-AuNPs (upper table). Specifically, the C atomic concentration increases from 40.9% to 55.9%, the N atomic concentration increases from 0.38% to 8.76% and the O atomic concentration from 0.83% to 5.07%. This high increase in these concentrations proves the presence of the polyA(NH_2 at 5' end) in the GO-AuNPs nanoplatform.

2.4.2 Raman spectra of GO-polyA(NH2 at 5' end, 20B), GO-polyA(SH at 5', 20B), GO

AuNPs are commonly used in SERS applications because their optical properties can be easily tuned to match the wavelength of the excitation laser, maximizing signal enhancement. To illustrate the signal amplification effect provided by AuNPs, we also

grafted polyA strands onto the surface of free GO without AuNPs and measured the Raman spectra of polyA, including its thiol and amine derivatives. The experimental conditions remained the same as those used when incorporating AuNPs, except $HAuCl_4$ was excluded from the synthesis to avoid the formation of AuNPs. Figure 2.6 presents the Raman spectra of pure GO (blue spectrum), GO functionalized with polyA(SH, 20 bases) (black spectrum), and GO functionalized with polyA(NH_2, 20 bases) (red spectrum).

In the absence of AuNPs for signal enhancement, the spectra primarily show the characteristic GO bands: the D band at 1343 cm^{-1} and the G band at 1595 cm^{-1}, while the characteristic bands of adenine are not visible due to the lack of enhancement. However, after grafting the DNA onto the GO, spectral changes can be observed in the peak positions and relative intensities of the D and G bands. Specifically, for GO-polyA (SH, 20 bases), the D band shifts to 1315 cm^{-1}, and the G band shifts to 1597 cm^{-1}. Similarly, for GO-polyA (NH_2, 20 bases), the D band shifts to 1314 cm^{-1}, and the G band also appears at 1597 cm^{-1}. Additionally, there is a noticeable change in the D/G band intensity ratio. For pure GO, the D/G ratio is 1.03, while for GO-polyA (SH, 20 bases), this ratio increases to 1.15, and for GO-polyA (NH_2, 20 bases), it further rises to 1.18. The increase in the D/G intensity ratio suggests the introduction of more defects in the GO sheets.

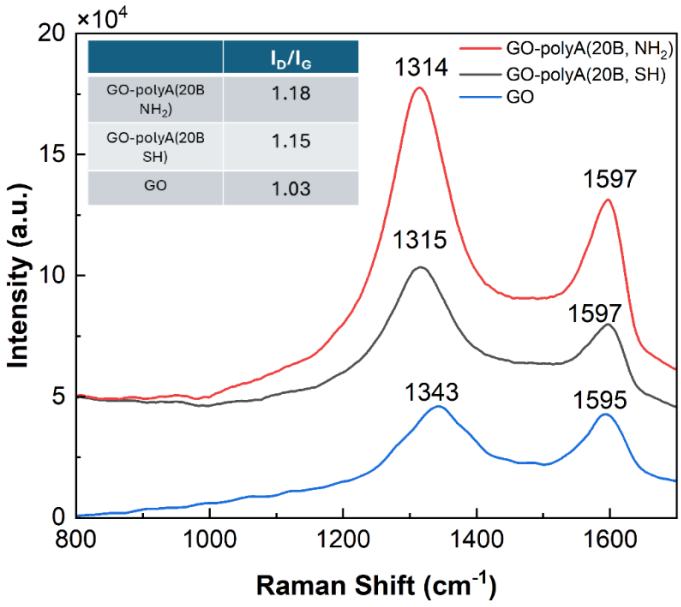

Figure 2.6. Raman spectrum of GO-polyA(20B, NH_2 at 5' end) (red spectrum), GO-polyA(20B SH at 5' end) (black spectrum) and GO (blue spectrum), Inset - table with the intensity ration between D and G band for each Raman Spectrum. Reprinted with permission from J. Phys. Chem. Lett. 2025, 16, 2, 435–442. Copyright 2025 American Chemical Society [24].

2.5. Detection of polyA strands using SERS

Further, this study focuses on the detection of DNA single strands. As mentioned above, I developed two different grafting methods for the polyA strands, one for the thiolate polyA which is grafted directly onto the AuNPs, and one for the NH_2-polyA which is grafted onto the graphene layers. Also, in each case we used four different lengths of the polyA strand: 5, 10, 15 and 20 bases which correspond to a total length of 4, 7.2, 10.4 and 14 nm, to see how the length influences the SERS spectra. The SERS spectra are presented in Figure 2.7. Figure 2.7a for GO-AuNPs-polyA(SH at 5' end) for all the lengths and Figure 2.7b for GO-AuNPs-polyA(NH_2 at 5' end). The concentration of polyA was kept the same at 10^{-6} M for each measurement. Also, we acquired around 20 spectra for each case, in Figure 2.7 being provide the average spectra.

In Figure 2.7, with pink, is represented the SERS spectra of GO-AuNPs with its two characteristics GO Raman peaks at 1326 cm^{-1} for the D band and at 1592 cm^{-1} for the G band [74], [75], [76], [77]. As can be seen, when polyA is being grafter onto the nanoplatform, different modifications in the spectra occurred. Firstly, we observe a change in the shape of the GO bands and also a shift, which means that in that region we have an overlap of bands from both GO and polyA. Also, in the region 700-1200 cm^{-1} new bands appeared which are all assigned to polyA. The most important polyA bands are the adenine ring breathing vibration which appeared at 732 cm^{-1} in case of GO-AuNPs-polyA(SH at 5' end) and at 732 cm^{-1} for GO-AuNPs-polyA(NH_2 at 5' end) (highlighted with blue in Figure 2.7a), and the backbone skeleton vibration which appears at 764 cm^{-1} for GO-AuNPs-polyA(SH at 5' end) and at 765 cm^{-1} for GO-AuNPs-polyA(NH_2 at 5' end) (highlighted with green in Figure 2.7b). I considered these two bands for quantitively measurements and PCA.

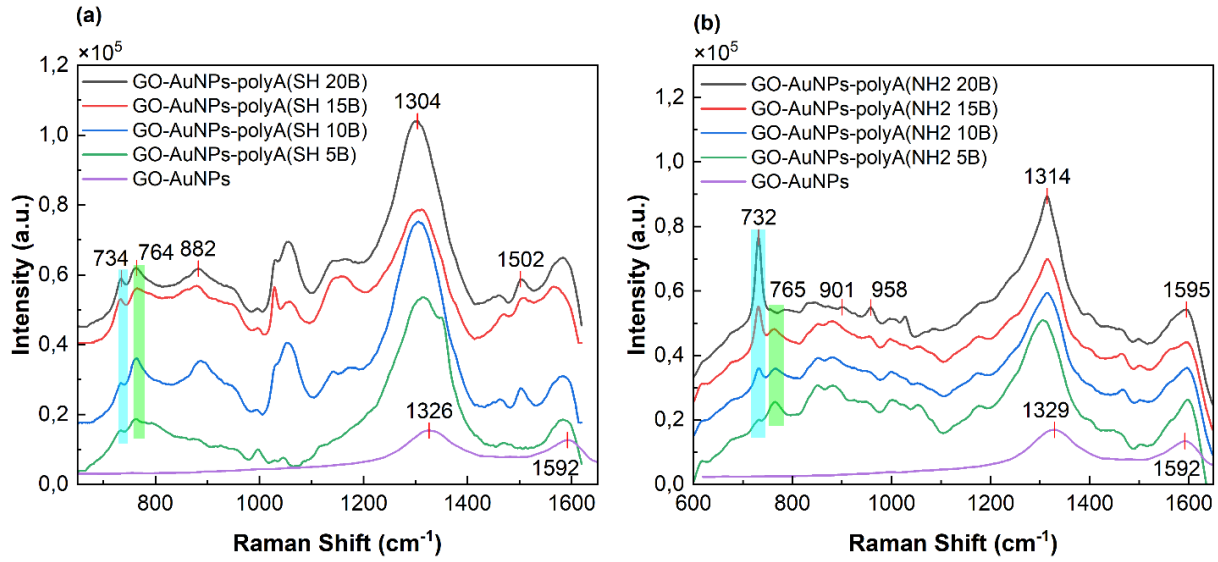

Figure 2.7. (a) SERS spectra of GO-AuNPs (purple spectrum) and GO-AuNPs-polyA (SH at 5') with polyA of different lengths: 20 bases (black spectrum), 15 bases (red spectrum), 10 bases (blue spectrum) and 5 bases (green spectrum); (b) SERS spectra of GO-AuNPs (purple spectrum) and GO-AuNPs-polyA (NH_2 at 5') with polyA of different lengths: 20 bases (black spectrum), 15 bases (red spectrum), 10 bases (blue spectrum). Reprinted with permission from J. Phys. Chem. Lett. 2025, 16, 2, 435–442. Copyright 2025 American Chemical Society [24].

2.5.1 GO-AuNPs-polyA(SH at 5' end) Nanoplatform

Let us begin by examining the GO-AuNPs-polyA(SH at 5' end) system. For this case, the polyA(SH at 5' end) strand is bonded through an SH bond direction onto the AuNP surface (Figure 2.8a). The 734 cm^{-1} peak decreases in its intensity as the number of bases in the polyA band decreases from 20 to 5. Specifically, a reduction in the peak intensity was detected as the strand length shortened, as shown in Figure 2.9 (represented by red dots, with Standard Deviation as Error). Each dot on the graph corresponds on x-axis to the distance between AuNPs surface and the terminal adenine base in the polyA strand. For this, we assumed a 0.63 nm spacing between two consecutive bases due to the nature of the ssDNA, along with a 0.92 nm spacer to account for the C6 linker and the thiol group attached at the 5' end of the strand, as described in prior studies [78]. As the number of adenine bases decreased from 20 to 15, there was a slightly drop in peak intensity. However, a significant reduction was observed when the number of bases decreased further to 10. Beyond this point, from 10 to 5, the intensity drop was gradual.

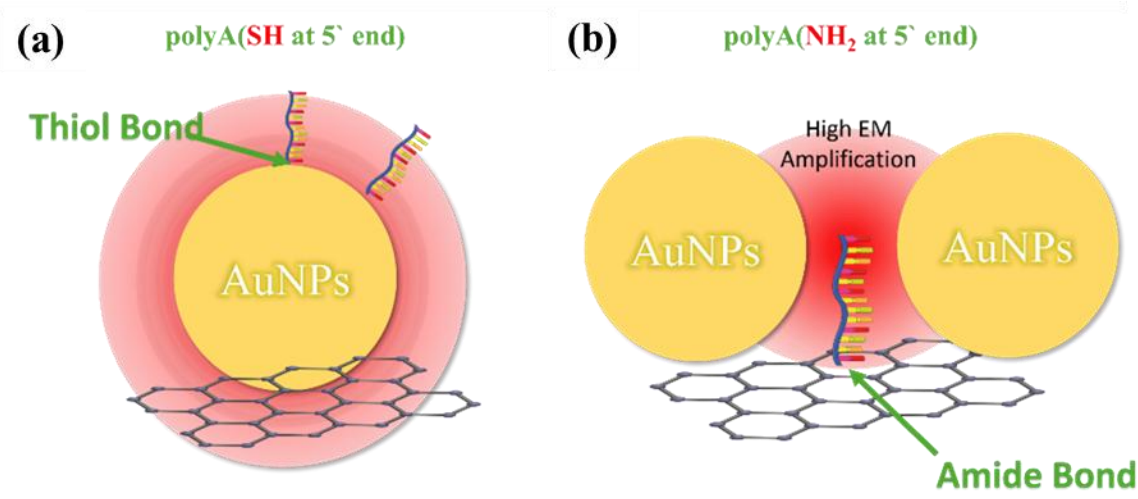

Figure 2.8. Schematic illustrations showing the strategic positioning of the polyA strand on the AuNPs surface (a), and between AuNPs in *hot-spots* (b). Reprinted with permission from J. Phys. Chem. Lett. 2025, 16, 2, 435–442. Copyright 2025 American Chemical Society [24].

It is known in literature that the field enhancement of a AuNPs decrease exponentially with distance from its surface [79]. Thus, the SERS signal of different lengths of polyA should not have the trend seen in Figure 2.9. The field enhancement as a function of distance from the surface of a 34 nm AuNPs was theoretically calculated using FDTD simulations (Figure 2.10a).

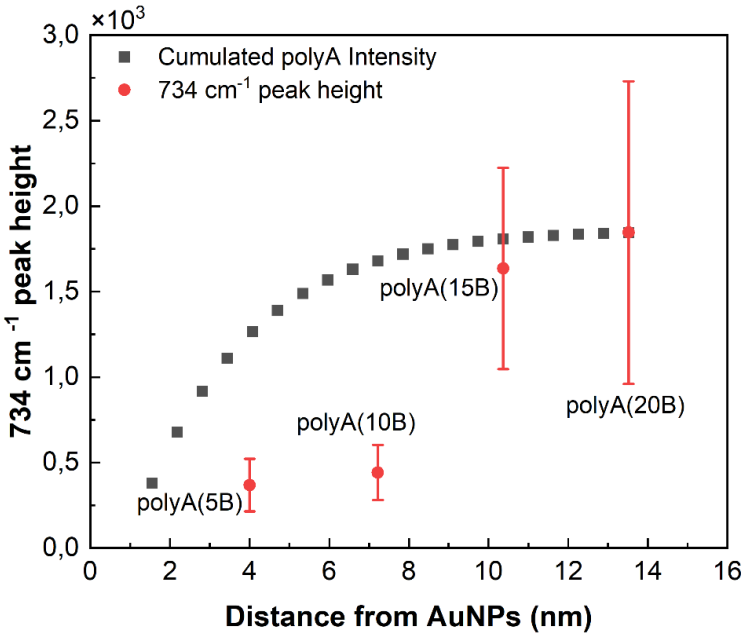

Figure 2.9. (a) Intensity of 734 cm^{-1} band of GO-AuNPs-polyA(SH at 5') for different number of bases (red dots), compared to the cumulated polyA intensity normalized to the 734 cm^{-1} band intensity for polyA (black square). Reprinted with permission from J. Phys. Chem. Lett. 2025, 16, 2, 435–442. Copyright 2025 American Chemical Society [24].

The exponentially decreasing field was extracted and shown in Figure 2.10b. In the case of short strands (5 and 10 bases), the bases are closer to the AuNPs, and their SERS signal is mainly influenced by the filed enhancement generated by the AuNPs surface to which the polyA(SH at 5' end) is bonded. However, the field intensity is very small overall, as seen in Figure 2.10b, thus a low SERS intensity of these strands is achieved. Conversely, for longer polyA strands (15 and 20 bases) we observed a significant increase in SERS signal, even though the additional adenine bases are farther away from the AuNPs surface, thus experiencing an even low field enhancement. This suggests that while individual bases further away from the surface contribute less to the overall SERS signal, the cumulative effect of multiple adenine bases compensate for this reduced enhancement. Essentially, the total SERS intensity reflects the additive contribution of each base in the polyA strand, with bases closer to the AuNPs surface having a greater impact on the overall study. To further analyze this effect, we simulated the total SERS intensity for polyA strands of varying lengths by summing the contributions of all the adenine bases, each weighted by their distance from the AuNP surface. By normalizing the enhanced electromagnetic field from Figure2.10b to 1, we calculated the corresponding field value for each base in the strand, depending on its distance from the nanoparticle surface. This is represented in Figure 2.9 (black squares). For instance, in the case of polyA strands with 20 bases, the contributions of all the adenine bases were summed up, leading to a substantial increase in the overall signal as the number of bases increased. This curve was then normalized to the value of the 734 cm^{-1} peak intensity of the GO-AuNPs-polyA(20B SH at 5' end). This trend is similar to the experimentally observed data, where the SERS signal increases with the length of the polyA strand. However, a notable deviation occurs between the two shorter strands (5 and 10 bases) and the two longer strands (15 and 20 bases). The SERS intensity for the 15- and 20-base polyA strands is significantly higher than that for the shorter strands and increase gradually following the theoretical path. This suggests that another factor may be contributing to the enhanced signal.

For the longer polyA(SH at 5' end) strands which have the lengths of approximately 10 and 13 nm for the 15-and 20-base strands, respectively, it is possible that the SERS signal to be influenced not only by the local field generated by the bound AuNP surface, but also by the fields of neighboring AuNPs. In such cases, longer DNA strands may interact with the plasmonic fields of adjacent AuNPs, leading to a greater overall enhancement of the SERS signal, as seen in Figure 2.9 red dots. Also, the standard deviation of the 734 cm^{-1}

band intensity, as seen in Figure 2.9 (red dots) shows a distinct trend: it is relatively low for the shorter polyA(SH at 5' end) strands, but significantly higher for the longer strands. This variation can be attributed to several factors. Firstly, the difference in standard deviation may stem from the changes in flexibility of the DNA strands with length. Shorter strands, such as those with 5 or 10 bases, are more rigid and restricted in the number of conformations they can adopt, leading to fewer possible orientations. In contrast, longer strands, like those with 15 or 20 bases, possess greater flexibility and can assume a wider range of conformations. This increased flexibility results in more varied orientations of the strand relative to the AuNP surface, causing a broader range of SERS signal intensities as the molecular orientation affects the efficiency of the signal enhancement. Additionally, the homogeneity of the electromagnetic field enhancement also plays a critical role in the observed signal variation. For the shorter polyA strands, the SERS signal is primarily generated by the field enhancement around a single AuNP, which even if it has low intensity, it has a high homogeneity. Since the shorter strands remain close to the surface of this one nanoparticle, the field enhancement is highly uniform, resulting in a more consistent and predictable SERS signal with a low standard deviation. For longer strands, 15 and 20 bases, their signal is influenced also by the field of neighboring AuNPs. Thus, the relative spatial arrangement and the distance between the strands and the AuNPs from vicinity leads to a high enhancement, but less homogeneous field. This inhomogeneity is measured by the high standard deviation which occurs only at the longer strands.

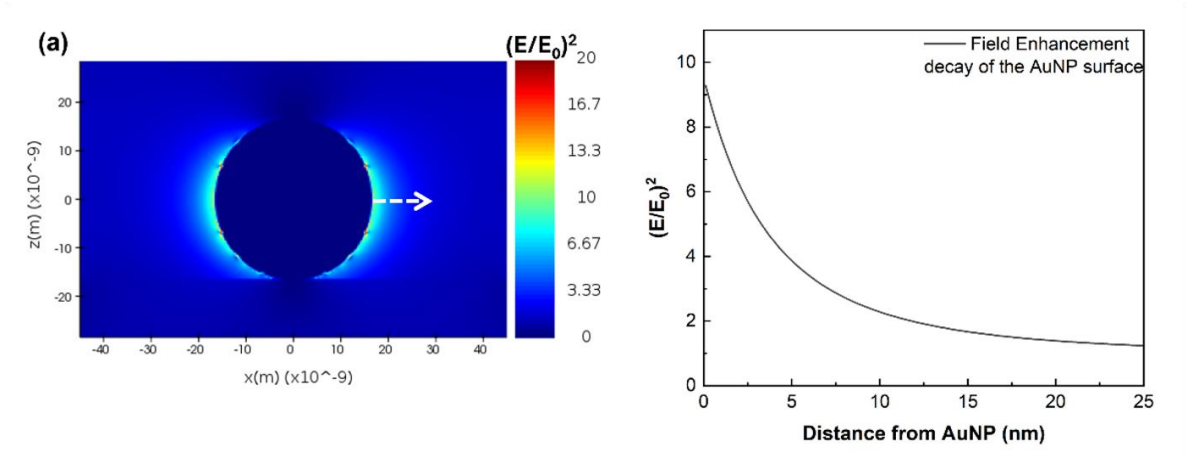

Figure 2.10. (a) FDTD field simulation of a 34 nm AuNPs; (b) Field Enhancement extracted from (a) in the direction of the which arrow. Reprinted with permission from J. Phys. Chem. Lett. 2025, 16, 2, 435–442. Copyright 2025 American Chemical Society [24].

Finally, we performed Principal Component Analysis (PCA) to check the intensity dispersibility of the two main bands: 734 and 764 cm^{-1}, to check if we can distinguish the signal coming from samples with different length of polyA(SH at 5' end) strand. The PCA was conducted on the range 700-800 cm^{-1} (Figure 2.11). The results revealed that the two major peaks were not well-separated by the analysis. The first principal component (PC1) is primarily associated with the 764 cm^{-1} band, though it also includes a minor contribution from the 734 cm^{-1} band. Conversely, the second principal component (PC2) is primarily linked to the 734 cm^{-1} band, with some contribution from the 764 cm^{-1} band. When examining the loading plot (Figure 2.11b), we observe that there is no distinct separation between the two principal components. In Figure 2.11 c and d, we plotted the average values of PC1 and PC2 for each case, along with their corresponding standard deviation. As seen in these plots, no specific trends emerge for either PC1 or PC2, and no correlation can be identified between the two principal components. This lack of correlation suggests that there is no direct relationship between the adenine signal (734 cm^{-1} band) and the phosphate backbone signal (764 cm^{-1} band).

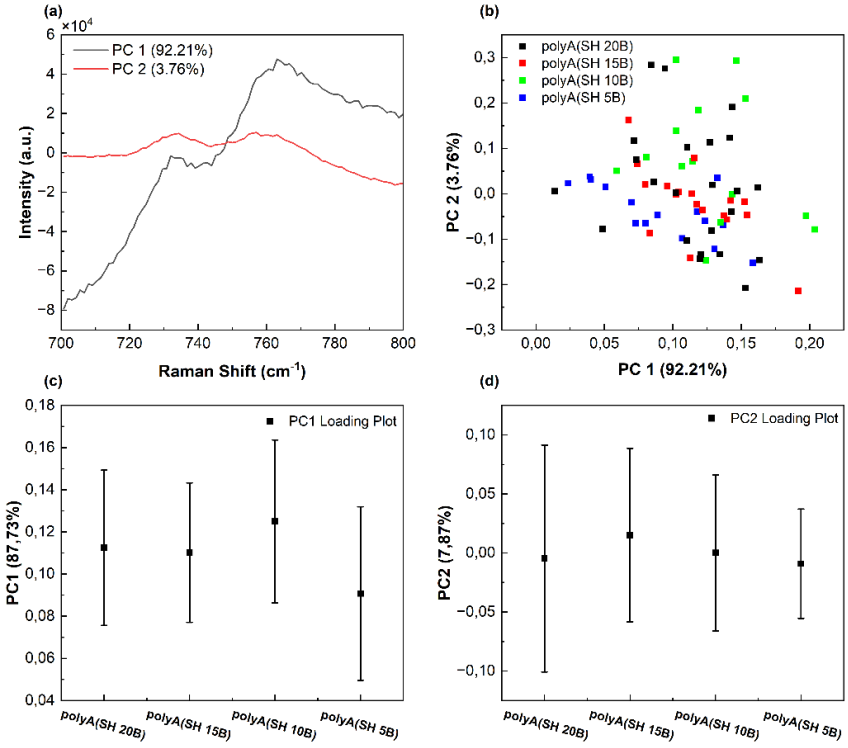

Figure 2.11. (a) Scores Plot of the GO-AuNPs-polyA(SH at 5' end) with different lengths; (b) Loading Plot of the GO-AuNPs-polyA(SH at 5' end) with different lengths of polyA; (c) The average PC1 value with standard deviation extracted from (b);(d) The average of PC2 value with standard deviation extracted from (b). Reprinted with permission from J. Phys. Chem. Lett. 2025, 16, 2, 435–442. Copyright 2025 American Chemical Society [24].

Consequently, we can infer that this particular DNA grafting method does not result in any preferential orientation of the DNA strand relative to the AuNP surface for different strand lengths. Instead, the DNA strand likely adopts a random conformation, with no specific alignment or structural order in relation to the AuNP surface.

2.5.2. GO-AuNPs-polyA(NH_2 at 5' end) nanoplatform

For the second grafting method, GO-AUNPs-polyA(NH_2 at 5' end) with various polyA strand length, the SERS spectra are shown in Figure 2.7b. We observed that for all lengths the adenine SERS signal is notably stronger in comparison with the GO-AuNPs-polyA(SH at 5' end). In this case, the polyA strand, functionalized with a NH_2 group at 5' end, forms an amid bond with the carboxylic groups of the GO, thus attaching directly onto the GO surface. It is known that the carboxylic groups in the GO are place at the edge of the graphene layer or in interior of the sheet where different defects occur, thus the polyA strands are attached to GO in both these places [80], [81], [82], [83].

When polyA strands and located near the edges, they are likely positioned close to individual AuNPs. However, if they bond within the interior of the GO layer, they may be situated within gaps between multiple AuNPs, creating localized *hot-spots,* as illustrated above in the Figure 2.8b. SEM images (Figure 2.4c) illustrate that the AuNPs tend to cluster on the GO sheets, forming dimers or larger aggregates, compared to free GO-AuNPs (Figure 2.4b). This clustering is also supported by the extinction spectrum (Figure 2.3b, black line), which shows a secondary plasmon band at 771 nm, indicative of nanoparticles aggregation. Also, in Figure 2.12 I performed a statistical analysis of the number of configurations, observed in multiple similar SEM images, with high SERS activity potential formed on the GO-AuNPs nanoplatform before and after the polyA(NH_2 at 5' end) grafting. These configurations correspond to the creation of active *hot-spots* inside the gaps between nanoparticles. Mainly, I counted for each case (before and after the polyA grafting) the number of isolated NPs, dimers, trimers or aggregates with more NPs. In total, I counted for GO-AuNPs about 2000 such configurations and for GO-AuNPs-polyA(NH_2 at 5' end) around 1600 configurations. As it can be seen in the histogram, before the grafting of the polyA(NH_2 at 5' end) 85% of the nanostructures were isolated AuNPs, while after the grafting the percentage dropped to 49%. Dimers increased from 9% to 23% for GO-AuNPs-polyA(NH_2 at 5' end) and the number of trimers also increased from 3% to 12%. There was an increase also for AuNPs configurations with 5 or more than 5 AuNPs. Therefore, numerous active

hot-spots are created after the incubation of the nanoplatform with polyA(NH_2 at 5' end), thus increasing the chances that the ssDNA molecules to occupy the optimum position for signal enhancement.

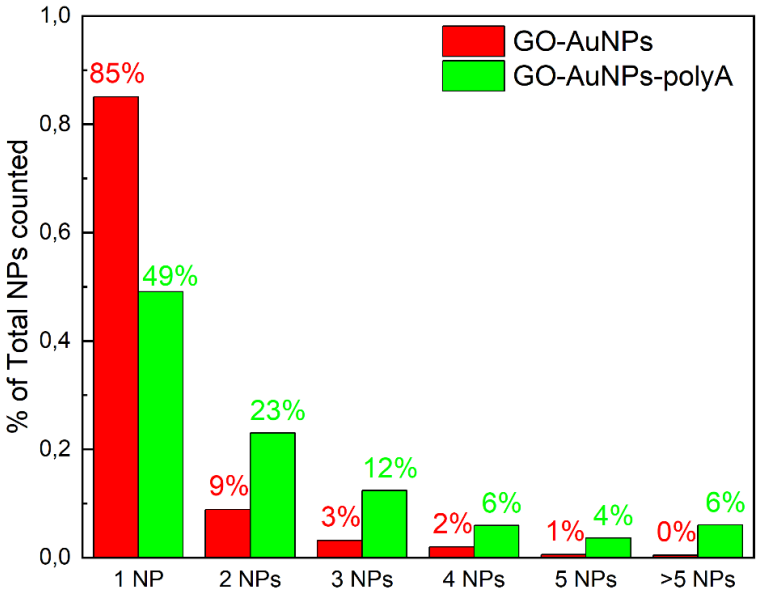

Figure 2.12. Statistical analysis of AuNPs nanoclusters before grafting the polyA(NH_2) (red) and after the grafting (green). Reprinted with permission from J. Phys. Chem. Lett. 2025, 16, 2, 435–442. Copyright 2025 American Chemical Society [24].

To determine qualitatively which are the chances that a molecule to be placed in a *hot-spot* I determined the ratio between the number of polyA(NH_2 at 5' end) and the number of AuNPs. Knowing that the molar mass of polyA is 6381.4 g/mol and a used volume of 10 µL at concentration 10^{-6} M, the number of polyA molecules is $6.023 \cdot 10^{12}$. I calculated the approximately number of AuNPs from the extinction spectra using the Beer-Lamber law:

$$A = \epsilon \cdot b \cdot C$$

where ε is the Extinction Coefficient, b is the optical path and C is the concentration. For this calculation, I used the experimental fitted extinction coefficient from Liu *et al.*[84]

$$\ln(\epsilon) = k \cdot \ln(D) + a$$

where k and a are fitted parameters and D is the diameter of the AuNPs, which in our case is 34 nm. The Molar Concentration has the following expression:

$$C_M = \frac{Nr\ of\ Moles}{Volume\ [L]} = \frac{Number\ of\ Particles}{Avogadro\ Number},$$

Finding the Nr of AuNPs to be around $3.6 \cdot 10^9$ results that in the solution I have approximately 1600 more polyA molecules than AuNPs. Therefore, even if considering that the probability of having polyA molecules strategically positioned in *hot-spots* is low, having an exceeding number of molecules compared to AuNPs makes our experimental findings feasible.

To model the field enhancement of the strands between coupled AuNPs, I conducted FDTD simulation using different gap sizes between coupled AuNPs, namely 2, 3 and 4 nm (Figure 2.13 a, b, c). I extracted the field enhancement and plotted separately in Figure 2.13 d. The point 0 on x-axis is represented by the (0,0) point in the images (Figure 2.13 a, b and c) and the field was extracted in the direction of negative z-axis. As can be seen, the field decays exponentially with the distance for all the three cases.

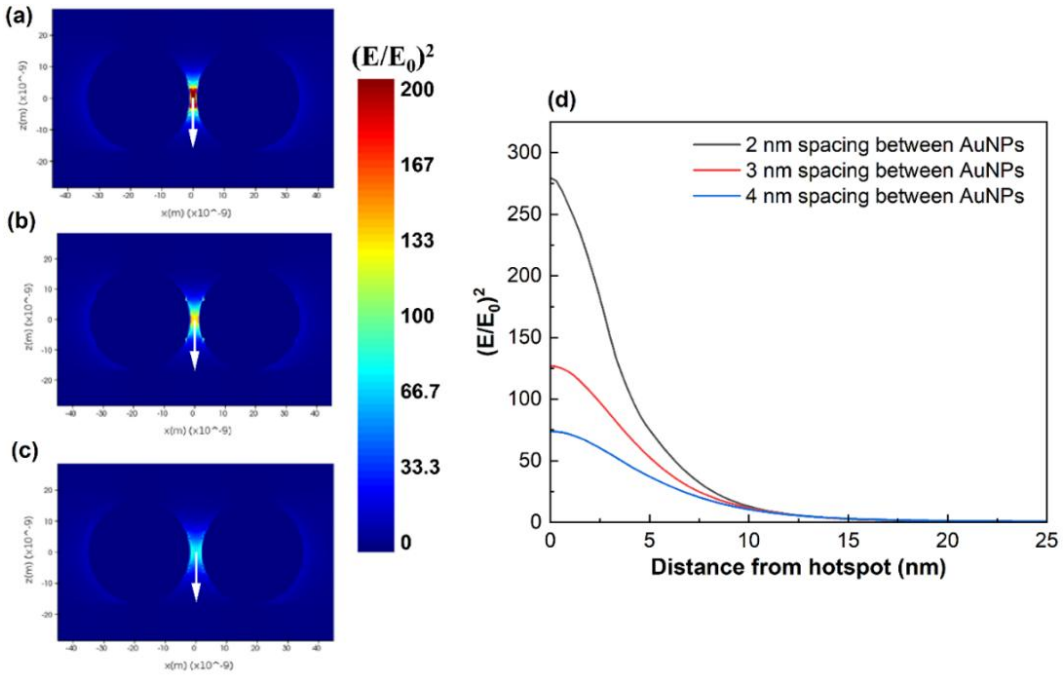

Figure 2.13. (a) FDTD simulation of coupled AuNPs with 2 nm gap size; (b) FDTD simulation of coupled AuNPs with 3 nm gap size; (c) FDTD simulation of Coupled AuNPs with 4 nm gap size; (d) Field extracted from (a), (b) and (c) as a distance from the point (0;0) in the negative Z direction. Reprinted with permission from J. Phys. Chem. Lett. 2025, 16, 2, 435–442. Copyright 2025 American Chemical Society [24].

Moreover, these simulations suggest that the field remains considerably higher than the previous case of one AuNPs (Figure 2.10) even for 4 nm gap. Specifically, the field is roughly 27 times stronger for 2 nm gap, 13 times stronger for 3 nm gap and 7 times stronger for 4 nm gap than isolated AuNPs. Further increasing the distance between coupled AuNPs we will obtain the limit case of two isolated AuNPs. This means that when polyA strands are

positioned in gaps between coupled AuNPs, their SERS signals dominate, while contributions from polyA near isolated AuNPs become negligible. This enhanced SERS intensity observed with the GO-AuNPs-polyA(NH_2 at 5' end) configuration is largely due to the positioning of the polyA strands in these *hot-spots* where the field enhancement is maximized and decays exponentially with distance from the AuNPs. FDTD simulation confirms the exponentially decreasing field effect.

As seen from the histogram (Figure 2.12), after the addition of polyA, not only the dimer configuration increases, but aggregates with a larger number of AuNPs increases too. Therefore, I conducted FDTD simulation on an aggregated nanostructure (Figure 2.14). Here, I modeled 7 different AuNPs with diameter between 20 and 33 nm with gap distances between 2 and 6 nm (Figure 2.14 a). In Figure 2.14 b I extracted the plane (a) and in Figure 2.14 c I plotted the field enhancement from Figure 2.14 b in the direction of the white arrows. As can be seen, the field enhancement between AuNPs is higher than in the case of surface field enhancement from isolated AuNPs, therefore regardless of the position of polyA molecules inside the AuNPs cluster, the SERS signal will be higher than in the polyA(SH at 5' end) case, where the DNA strand is attached to isolated AuNPs.

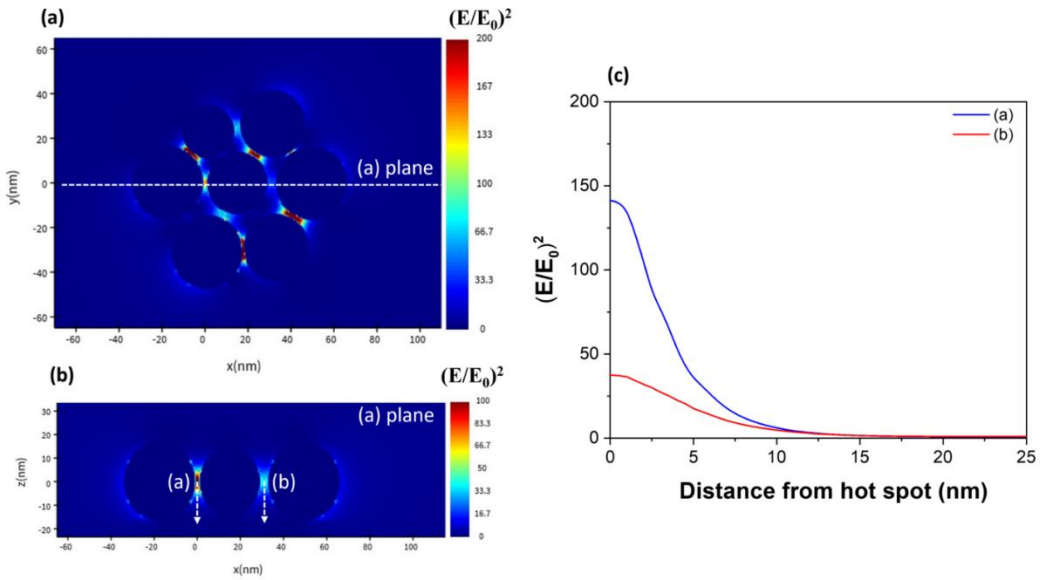

Figure 2.14. (a) FDTD simulation of AuNPs aggregates composed of 7 AuNPs with diameters between 20 and 35 nm with gap distance between 1 and 7 nm. Reprinted with permission from J. Phys. Chem. Lett. 2025, 16, 2, 435–442. Copyright 2025 American Chemical Society [24].

Furthermore, the broad band at 771 nm in (Figure 2.3b black spectrum), observed after polyA(NH_2 at 5' end) grafting, supports the likelihood of polyA strands being

positioned within these gaps due to nanoparticle aggregation. Hence, we attribute the high SERS intensities observed with GO-AuNPs-polyA(NH_2) to the placement of the polyA strands between AuNPs, directly within *hot-spots*.

By examining the 732 cm^{-1} band, we observe an exponential decrease in intensity with decreasing polyA(NH_2) strand length. Figure 2.15 (red dots) with Standard Deviation as yError shows the band intensities for different polyA(NH_2) lengths, with each point representing the location of the last adenine base in the strand relative to the center of the *hot-spot*. As the number of bases decreases, the DNA strand shortens, resulting in fewer adenine bases in the high-field *hot-spots,* which in turn reduces the enhancement and causes the SERS intensity to decrease exponentially.

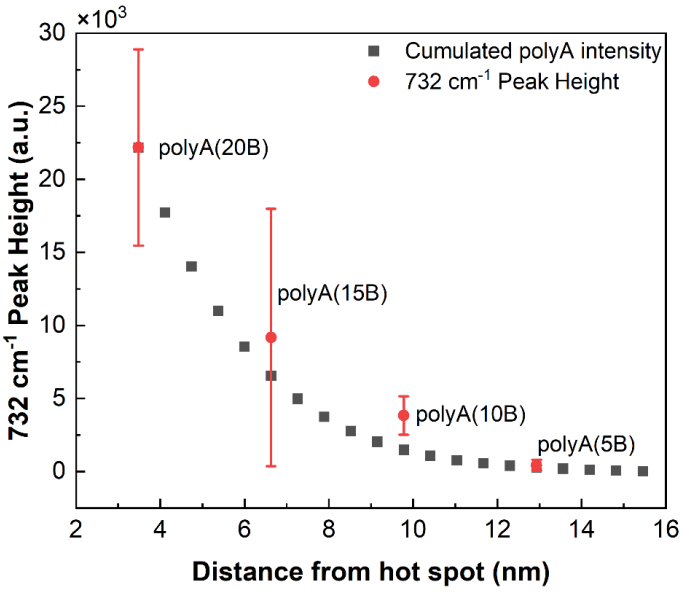

Figure 2.15. Intensity of 732 cm^{-1} band of GO-AuNPs-polyA(NH_2 at 5') for different number of bases (red dots), compared to the cumulated polyA intensity normalized to the 732 cm^{-1} band intensity for polyA (black square); Reprinted with permission from J. Phys. Chem. Lett. 2025, 16, 2, 435–442. Copyright 2025 American Chemical Society [24].

As for the GO-AuNPs-polyA(SH at 5' end), I conducted calculations regarding the cumulative SERS signal of the different lengths considering the overall contribution of the polyA(NH_2) bases in the field enhancement produced by the coupled AuNPs. For this calculation I used the field values from the 2 nm gap dimers (Figure 2.14d, blue curve). I normalized to 1 the field enhancement and extracted the weight for each distance corresponding to each adenine base in the sequence. I calculated the SERS contribution for

each strand and added them together. The cumulative intensity was then normalized to the peak height of the 732 cm^{-1} GO-AuNPs-polyA(20B, NH_2 at 5' end). The cumulative intensity is represented in Figure 2.15, black squares. As can be seen, the intensity decreases exponentially with decreasing the number of bases and it is in very good agreement with the experimental data (Figure 2.15, red squares) validating our assumption on the strategic placement of the polyA(NH_2) strand inside the *hot-spot.*

The distribution of the 732 and 764 cm^{-1} bands intensity was calculated using PCA, with the resulting Scores and Loading Plots displayed in Figure 2.16 a and b, respectively. Compared to the GO-AuNPs-polyA(SH at 5' end) nanoplatform (Figure 2.11), this PCA analysis better differentiates the two main bands: here PC1 is dominated only by the 732 cm^{-1} band's contribution to the SERS spectrum, while PC2 represents the 764 cm^{-1} band, as can be seen from Figure 2.16a. We plotted separately the PC1 and PC2 in Figure 2.16 c and d respectively alongside with their standard deviation as yError. For this particular grafting method, we observe a clear relationship between the principal component scores and the polyA(NH_2 at 5' end) strand length. As shown, the PC1 score increases with polyA length, while the PC2 score increases has a opposite trend, decreasing with polyA length. Also, we can observe that in both cases, the standard deviation is higher for longer strands (15 and 20 bases) and lower for shorter strands (10 and 5 bases).

This trend can be attributed to two main factors: DNA flexibility and the localized field enhancement. First, as the DNA strand lengthens, its increases flexibility allows it to assume various positions within the *hot-spot*, where the field enhancement is strongest. Because the electromagnetic field in this region is highly localized and the gradient of the field is high, even small changes in the adenine base's position can cause significant variations in the SERS signal, resulting in a larger deviation around the mean intensity. In contrast, shorter DNA strands are less flexible and tend to occupy regions with lower field enhancement and lower field gradient, making the SERS signal less sensitive to small orientation or conformation changes, thereby producing a lower signal deviation.

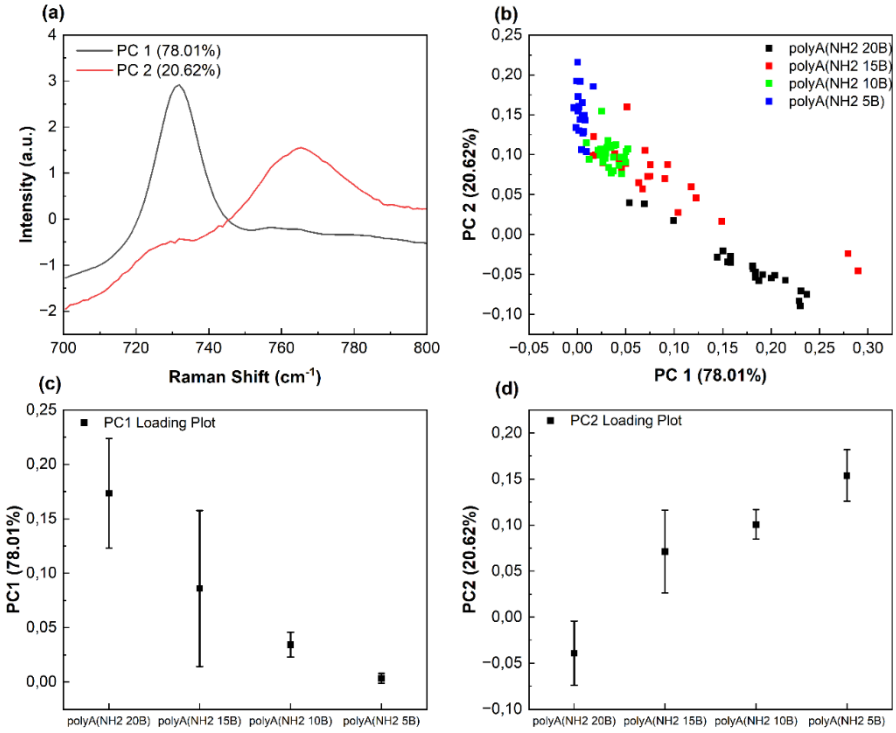

Figure 2.16 (a) Scores Plot – PC1 and PC2 components of GO-AuNPs-polyA(NH_2 at 5' end) with 20, 15, 10 and 5 number of bases. (b) Loading Plot of GO-AuNPs-polyA(NH_2 at 5' end) with 20, 15, 10 and 5 number of bases. (c) PC1 Average with standard deviation as yError. (d) PC2 Average with standard deviation as yError. Reprinted with permission from J. Phys. Chem. Lett. 2025, 16, 2, 435–442. Copyright 2025 American Chemical Society [24].

The Loading Plot (Figure 2.16d) clearly highlights an inverse correlation between PC1 and PC2 contributions, further emphasizing the differential influence of each principal component. This indicates that shorter strands (5 and 10 bases) yield SERS spectra dominated by the DNA backbone, while longer strands are more heavily influenced by the adenine signal. When the DNA strand, particularly at a length of 20 bases, is positioned directly within the *hot-spot*, the adenine bases are oriented perpendicularly to the AuNP surface and parallel to the electromagnetic field, maximizing the signal enhancement. Conversely, when the DNA strand lies outside the *hot-spot*, the adenine is no longer optimally oriented relative to the enhanced field, and thus, the backbone signal predominates in the SERS spectrum. Therefore, for this particular grafting method of the polyA(NH_2 at 5' end) onto the GO-AuNPs nanoplatform there is a clear correlation between the PCA results and the strand length suggesting a stable and reproducible orientation of the DNA strand within the *hot-spots* allowing for consistent signal enhancement based on length and positioning.

Conclusions

This study successfully highlights how the SERS signal of polyA strands depends on both strand length and the type of chemical bond formed with the GO-AuNP nanoplatform. These results show that the GO-AuNPs-polyA(NH_2 at the 5' end) nanoplatform generates a significantly stronger adenine signal compared to the GO-AuNPs-polyA(SH at the 5' end). This enhancement arises from the covalent bonding of the polyA(NH_2 at the 5' end) strand to GO via an amide bond, which positions it between coupled AuNPs in *hot-spots* where the local field amplification is higher.

Additionally, we examined how the polyA SERS signal varies with strand length for each nanoplatform by measuring polyA strands of 5, 10, 15, and 20 bases. For GO-AuNPs-polyA(SH at the 5' end), we observed that the contribution to the SERS signal depends on strand length. Shorter strands (5 and 10 bases) remain in the weaker field regions of the AuNPs to which they are attached, leading to lower signal intensity and minimal variation. However, as the strand length increases (15 and 20 bases), the polyA strand extends into different field regions of neighboring AuNPs, significantly enhancing the signal intensity. The random arrangement of AuNPs affects the total field experienced by the strand, contributing to the greater variability in SERS signal for longer strands.

For GO-AuNPs-polyA(NH_2 at the 5' end), the adenine strand is strategically positioned within the *hot-spot* between AuNPs, where field enhancement is strongest. As strand length increases, a larger portion of the polyA sequence remains within the high-intensity field, further amplifying the signal. We demonstrate that the intensity of the adenine peak at 732 cm^{-1} exhibits an exponential increase with strand length. Additionally, we observed an inverse correlation between the 765 cm^{-1} peak and the 732 cm^{-1} peak. By systematically varying polyA strand lengths and positioning them within *hot-spots* I succeeded to probe the local field enhancement of plasmonic coupled AuNPs.

References

[1] W. S. Jr. Hummers and R. E. Offeman, "Preparation of Graphitic Oxide," *J. Am. Chem. Soc.*, vol. 80, no. 6, pp. 1339–1339, Mar. 1958, doi: 10.1021/ja01539a017.
[2] Y. Sun *et al.*, "In situ synthesis of graphene oxide/gold nanocomposites as ultrasensitive surface-enhanced Raman scattering substrates for clenbuterol detection," *Anal. Bioanal. Chem.*, vol. 412, no. 1, pp. 193–201, Jan. 2020, doi: 10.1007/s00216-019-02230-1.
[3] F. Tian, F. Bonnier, A. Casey, A. E. Shanahan, and H. J. Byrne, "Surface enhanced Raman scattering with gold nanoparticles: effect of particle shape," *Anal. Methods*, vol. 6, no. 22, pp. 9116–9123, Oct. 2014, doi: 10.1039/C4AY02112F.
[4] J. Langer *et al.*, "Present and Future of Surface-Enhanced Raman Scattering," *ACS Nano*, vol. 14, no. 1, pp. 28–117, Jan. 2020, doi: 10.1021/acsnano.9b04224.
[5] X. X. Han, R. S. Rodriguez, C. L. Haynes, Y. Ozaki, and B. Zhao, "Surface-enhanced Raman spectroscopy," *Nat. Rev. Methods Primer*, vol. 1, no. 1, pp. 1–17, Jan. 2022, doi: 10.1038/s43586-021-00083-6.
[6] D. Ayrat, *Graphene Oxide. Fundamentals and Applications*. Wiley, 2017.
[7] D. R. Dreyer, S. Park, C. W. Bielawski, and R. S. Ruoff, "The chemistry of graphene oxide," *Chem. Soc. Rev.*, vol. 39, no. 1, pp. 228–240, Jan. 2010, doi: 10.1039/b917103g.
[8] V. Kansara and M. Patel, "Exploring the role of graphene-metal hybrid nanomaterials as Raman signal enhancers in early stage cancer detection," *Talanta*, vol. 283, p. 127185, Feb. 2025, doi: 10.1016/j.talanta.2024.127185.
[9] X. Fu, F. Bei, X. Wang, S. O'Brien, and J. R. Lombardi, "Excitation profile of surface-enhanced Raman scattering in graphene–metal nanoparticle based derivatives," *Nanoscale*, vol. 2, no. 8, pp. 1461–1466, Aug. 2010, doi: 10.1039/C0NR00135J.
[10] F. A. Deader, Y. Abbas, A. Qurashi, M. Al-Qutayri, V. Chan, and M. Rezeq, "Electric Field-Driven Self-Assembly of Gold Nanoparticle Monolayers on Silicon Substrates," *Langmuir*, vol. 39, no. 44, pp. 15766–15772, Nov. 2023, doi: 10.1021/acs.langmuir.3c02351.
[11] I. Khalil, N. M. Julkapli, W. A. Yehye, W. J. Basirun, and S. K. Bhargava, "Graphene–Gold Nanoparticles Hybrid—Synthesis, Functionalization, and Application in a Electrochemical and Surface-Enhanced Raman Scattering Biosensor," *Materials*, vol. 9, no. 6, p. 406, May 2016, doi: 10.3390/ma9060406.
[12] W. Zhao *et al.*, "Raman Enhancement Caused by Gold Nanoparticles Clustered Between Graphene and Substrate," *J. Nanosci. Nanotechnol.*, vol. 15, no. 4, pp. 3173–3177, Apr. 2015, doi: 10.1166/jnn.2015.9646.
[13] X. Liang *et al.*, "Tuning plasmonic and chemical enhancement for SERS detection on graphene-based Au hybrids," *Nanoscale*, vol. 7, no. 47, pp. 20188–20196, Nov. 2015, doi: 10.1039/C5NR06010A.
[14] X. Ling *et al.*, "Can Graphene be used as a Substrate for Raman Enhancement?," *Nano Lett.*, vol. 10, no. 2, pp. 553–561, Feb. 2010, doi: 10.1021/nl903414x.
[15] L. Dolgov *et al.*, "Graphene-Enhanced Raman Scattering from the Adenine Molecules," *Nanoscale Res. Lett.*, vol. 11, no. 1, p. 197, Apr. 2016, doi: 10.1186/s11671-016-1418-5.
[16] W. Yang *et al.*, "Graphene-Ag nanoparticles-cicada wings hybrid system for obvious SERS performance and DNA molecular detection," *Opt. Express*, vol. 27, no. 3, Art. no. 3, Feb. 2019, doi: 10.1364/OE.27.003000.

[17] A. A. Babadi *et al.*, "SARS-CoV-2 detection by targeting four loci of viral genome using graphene oxide and gold nanoparticle DNA biosensor," *Sci. Rep.*, vol. 12, no. 1, Art. no. 1, Nov. 2022, doi: 10.1038/s41598-022-23996-y.
[18] D. Gao *et al.*, "On-line SERS detection of adenine in DNA based on the optofluidic in-fiber integrated GO/PDDA/Ag NPs," *Sens. Actuators B Chem.*, vol. 332, p. 129517, Apr. 2021, doi: 10.1016/j.snb.2021.129517.
[19] S. Heinsalu *et al.*, "Silver nanoparticles with reduced graphene oxide for surface-enhanced vibrational spectroscopy of DNA constituents," *Appl. Nanosci.*, vol. 9, no. 5, Art. no. 5, Jul. 2019, doi: 10.1007/s13204-018-0924-4.
[20] E. Avci *et al.*, "Label-Free Surface Enhanced Raman Spectroscopy for Cancer Detection," *Cancers*, vol. 14, no. 20, Art. no. 20, Oct. 2022, doi: 10.3390/cancers14205021.
[21] U. S. Inan and R. A. Marshall, "Introduction," in *Numerical Electromagnetics. The FDTD Method*, Cambridge University Press, 2011.
[22] Y. Hao and R. Mittra, "A Bief Introduction to the FDTD Method for Moedeling Nanomaterials," in *FDTD Modeling of Metamaterials. Theory and Applications*, Artech House, 2009, pp. 67–88.
[23] "What is Finite-Difference Time-Domain (FDTD)?" Accessed: Oct. 28, 2024. [Online]. Available: https://www.ansys.com/blog/what-is-fdtd
[24] V. Cucuiet *et al.*, "Probing the Local Field Enhancement Using SERS Detection of DNA Strands with Different Lengths and Grafting Strategies on Graphene Oxide Plasmonic Nanoplatforms," *J. Phys. Chem. Lett.*, pp. 435–442, Dec. 2024, doi: 10.1021/acs.jpclett.4c02529.
[25] V. Cucuiet, D. Maniu, S. Astilean, M. Lamy de la Chapelle, and M. Focsan, "Graphene-mediated surface enhanced Raman spectroscopy for DNA Detection&hybridization: Breakthroughs and challenges," *Biosens. Bioelectron.*, vol. 286, p. 117610, Oct. 2025, doi: 10.1016/j.bios.2025.117610.
[26] A. Holca, V. Cucuiet, S. Astilean, M. L. de la Chapelle, and M. Focsan, "Recent advances in gold nanoparticle-graphene hybrid nanoplatforms with visible to near-infrared response for photodynamic and photothermal therapy and bioimaging," *RSC Adv.*, vol. 15, no. 15, pp. 11902–11922, 2025, doi: 10.1039/D4RA09100K.
[27] R. R. Jones, D. C. Hooper, L. Zhang, D. Wolverson, and V. K. Valev, "Raman Techniques: Fundamentals and Frontiers," *Nanoscale Res. Lett.*, vol. 14, no. 1, p. 231, Jul. 2019, doi: 10.1186/s11671-019-3039-2.
[28] A. Orlando *et al.*, "A Comprehensive Review on Raman Spectroscopy Applications," *Chemosensors*, vol. 9, no. 9, Art. no. 9, Sep. 2021, doi: 10.3390/chemosensors9090262.
[29] M. User:Pavlina2.0 based on work of, *English: Molecular energy levels and Raman effect*. 2009. Accessed: Jan. 12, 2025. [Online]. Available: https://commons.wikimedia.org/wiki/File:Raman_energy_levels.svg
[30] M. Fleischmann, P. J. Hendra, and A. J. McQuillan, "Raman spectra of pyridine adsorbed at a silver electrode," *Chem. Phys. Lett.*, vol. 26, no. 2, pp. 163–166, May 1974, doi: 10.1016/0009-2614(74)85388-1.
[31] D. L. Jeanmaire and R. P. Van Duyne, "Surface raman spectroelectrochemistry: Part I. Heterocyclic, aromatic, and aliphatic amines adsorbed on the anodized silver electrode," *J. Electroanal. Chem. Interfacial Electrochem.*, vol. 84, no. 1, pp. 1–20, Nov. 1977, doi: 10.1016/S0022-0728(77)80224-6.
[32] R. Chen and L. Jensen, "Interpreting chemical enhancements of surface-enhanced Raman scattering," *Chem. Phys. Rev.*, vol. 4, no. 2, p. 021305, May 2023, doi: 10.1063/5.0138501.

[33] W.-H. Park and Z. H. Kim, "Charge Transfer Enhancement in the SERS of a Single Molecule," *Nano Lett.*, vol. 10, no. 10, pp. 4040–4048, Oct. 2010, doi: 10.1021/nl102026p.
[34] N. Valley, N. Greeneltch, R. P. Van Duyne, and G. C. Schatz, "A Look at the Origin and Magnitude of the Chemical Contribution to the Enhancement Mechanism of Surface-Enhanced Raman Spectroscopy (SERS): Theory and Experiment," *J. Phys. Chem. Lett.*, vol. 4, no. 16, pp. 2599–2604, Aug. 2013, doi: 10.1021/jz4012383.
[35] N. Valley, L. Jensen, J. Autschbach, and G. C. Schatz, "Theoretical studies of surface enhanced hyper-Raman spectroscopy: The chemical enhancement mechanism," *J. Chem. Phys.*, vol. 133, no. 5, p. 054103, Aug. 2010, doi: 10.1063/1.3456544.
[36] S. M. Morton and L. Jensen, "Understanding the Molecule−Surface Chemical Coupling in SERS," *J. Am. Chem. Soc.*, vol. 131, no. 11, pp. 4090–4098, Mar. 2009, doi: 10.1021/ja809143c.
[37] J. R. Lombardi, "The theory of surface-enhanced Raman scattering on semiconductor nanoparticles; toward the optimization of SERS sensors," *Faraday Discuss.*, vol. 205, pp. 105–120, 2017, doi: 10.1039/C7FD00138J.
[38] M. Aftab, M. S. Mansha, T. Iqbal, and M. Farooq, "Surface Plasmon Excitation: Theory, Configurations, and Applications," *Plasmonics*, vol. 19, no. 4, pp. 1701–1719, Aug. 2024, doi: 10.1007/s11468-023-02095-2.
[39] S. Maier, "Enhancement of emissive processes and nonlinearities," in *Plasmonics: Funcamentals and Applications*, Springer Science, 2007, pp. 159–175.
[40] "Surface enhanced Raman scattering (SERS) by molecules adsorbed at spherical particles: errata." Accessed: Jan. 16, 2025. [Online]. Available: https://opg.optica.org/ao/abstract.cfm?uri=ao-19-24-4159
[41] "Biosensors | Free Full-Text | A Review on Surface-Enhanced Raman Scattering." Accessed: Sep. 12, 2024. [Online]. Available: https://www.mdpi.com/2079-6374/9/2/57
[42] K. P. F. Janssen, K. Knez, D. Spasic, and J. Lammertyn, "Nucleic Acids for Ultra-Sensitive Protein Detection," *Sensors*, vol. 13, no. 1, Art. no. 1, Jan. 2013, doi: 10.3390/s130101353.
[43] N. R. C. (US) C. on D. F. S. A. Update, "Genetic and Molecular Basis of DNA Typing," in *The Evaluation of Forensic DNA Evidence*, National Academies Press (US), 1996. Accessed: Sep. 12, 2024. [Online]. Available: https://www.ncbi.nlm.nih.gov/books/NBK232609/
[44] S. Zangana, M. Veres, and A. Bonyár, "Surface-Enhanced Raman Spectroscopy (SERS)-Based Sensors for Deoxyribonucleic Acid (DNA) Detection," *Molecules*, vol. 29, no. 14, Art. no. 14, Jan. 2024, doi: 10.3390/molecules29143338.
[45] L. Zou, R. Shen, L. Ling, and G. Li, "Sensitive DNA detection by polymerase chain reaction with gold nanoparticles," *Anal. Chim. Acta*, vol. 1038, pp. 105–111, Dec. 2018, doi: 10.1016/j.aca.2018.07.006.
[46] D. Khodakov, J. Li, J. X. Zhang, and D. Y. Zhang, "Highly multiplexed rapid DNA detection with single-nucleotide specificity via convective PCR in a portable device," *Nat. Biomed. Eng.*, vol. 5, no. 7, Art. no. 7, Jul. 2021, doi: 10.1038/s41551-021-00755-4.
[47] N. Harikai, Y. Tanaka, S. Miyashita, K. Zaima, and K. Shinomiya, "Real-time PCR Method for Detection of Short DNA using a Deoxyuridine Probe and Application for Detection of Fomivirsen," *BioTechniques*, vol. 73, no. 6, Art. no. 6, Dec. 2022, doi: 10.2144/btn-2022-0068.

[48] D. Chang *et al.*, "Detection of DNA Amplicons of Polymerase Chain Reaction Using Litmus Test," *Sci. Rep.*, vol. 7, no. 1, Art. no. 1, Jun. 2017, doi: 10.1038/s41598-017-03009-z.
[49] N. Mahdieh and B. Rabbani, "An Overview of Mutation Detection Methods in Genetic Disorders," *Iran. J. Pediatr.*, vol. 23, no. 4, pp. 375–388, Aug. 2013.
[50] A. Kowalczyk *et al.*, "New strategy for the gene mutation identification using surface enhanced Raman spectroscopy (SERS)," *Biosens. Bioelectron.*, vol. 132, pp. 326–332, May 2019, doi: 10.1016/j.bios.2019.03.019.
[51] T. Vo-Dinh, L. R. Allain, and D. L. Stokes, "Cancer gene detection using surface-enhanced Raman scattering (SERS)," *J. Raman Spectrosc.*, vol. 33, no. 7, pp. 511–516, 2002, doi: 10.1002/jrs.883.
[52] L. Wu *et al.*, "Profiling DNA mutation patterns by SERS fingerprinting for supervised cancer classification," *Biosens. Bioelectron.*, vol. 165, p. 112392, Oct. 2020, doi: 10.1016/j.bios.2020.112392.
[53] W. Xu, N. Mao, and J. Zhang, "Graphene: A Platform for Surface-Enhanced Raman Spectroscopy," *Small*, vol. 9, no. 8, pp. 1206–1224, 2013, doi: 10.1002/smll.201203097.
[54] H. Lai, F. Xu, Y. Zhang, and L. Wang, "Recent progress on graphene-based substrates for surface-enhanced Raman scattering applications," *J. Mater. Chem. B*, vol. 6, no. 24, pp. 4008–4028, 2018, doi: 10.1039/C8TB00902C.
[55] S. Feng *et al.*, "Ultrasensitive molecular sensor using N-doped graphene through enhanced Raman scattering," *Sci. Adv.*, vol. 2, no. 7, p. e1600322, Jul. 2016, doi: 10.1126/sciadv.1600322.
[56] Y. Fu *et al.*, "Graphene related materials for thermal management," *2D Mater.*, vol. 7, no. 1, p. 012001, Oct. 2019, doi: 10.1088/2053-1583/ab48d9.
[57] J. Li, J. Liu, N. Li, W. Zeng, M. Chen, and Y. Xu, "High thermal conductivity graphene-based interfacial materials through oriented assembly and catalytic graphitization for thermal management," *Carbon*, vol. 235, p. 120081, Mar. 2025, doi: 10.1016/j.carbon.2025.120081.
[58] L. Liu *et al.*, "Graphene-based polymer composites in thermal management: materials, structures and applications," *Mater. Horiz.*, vol. 12, no. 1, pp. 64–91, Jan. 2025, doi: 10.1039/D4MH00846D.
[59] S. Gupta and A. Banaszak, "Detection of DNA bases and environmentally relevant biomolecules and monitoring ssDNA hybridization by noble metal nanoparticles decorated graphene nanosheets as ultrasensitive G-SERS platforms," *J. Raman Spectrosc.*, vol. 52, no. 5, pp. 930–948, 2021, doi: 10.1002/jrs.6087.
[60] S. Heinsalu *et al.*, "Silver nanoparticles with reduced graphene oxide for surface-enhanced vibrational spectroscopy of DNA constituents," *Appl. Nanosci.*, vol. 9, no. 5, pp. 1075–1083, Jul. 2019, doi: 10.1007/s13204-018-0924-4.
[61] X. Zhang, T. Gouriye, K. Göeken, M. R. Servos, R. Gill, and J. Liu, "Toward Fast and Quantitative Modification of Large Gold Nanoparticles by Thiolated DNA: Scaling of Nanoscale Forces, Kinetics, and the Need for Thiol Reduction," *J. Phys. Chem. C*, vol. 117, no. 30, Art. no. 30, Aug. 2013, doi: 10.1021/jp403946x.
[62] X. Ma, X. Li, G. Luo, and J. Jiao, "DNA-functionalized gold nanoparticles: Modification, characterization, and biomedical applications," *Front. Chem.*, vol. 10, Dec. 2022, doi: 10.3389/fchem.2022.1095488.
[63] K. C. Joy, "Functionalization of gold nanoparticles with thiolated DNA," Rutgers University - Graduate School - Camden, 2024. doi: 10.7282/t3-j855-q709.
[64] E. Papadopoulou and S. E. J. Bell, "Label-Free Detection of Nanomolar Unmodified Single- and Double-Stranded DNA by Using Surface-Enhanced Raman Spectroscopy

on Ag and Au Colloids," *Chem. – Eur. J.*, vol. 18, no. 17, Art. no. 17, 2012, doi: 10.1002/chem.201103520.
[65] Y. Zhu *et al.*, "A Poly Adenine-Mediated Assembly Strategy for Designing Surface-Enhanced Resonance Raman Scattering Substrates in Controllable Manners," *Anal. Chem.*, vol. 87, no. 13, Art. no. 13, Jul. 2015, doi: 10.1021/acs.analchem.5b00676.
[66] D. Li *et al.*, "Label-Free Detection of miRNA Using Surface-Enhanced Raman Spectroscopy," *Anal. Chem.*, vol. 92, no. 19, Art. no. 19, Oct. 2020, doi: 10.1021/acs.analchem.0c03335.
[67] S. Al-Zangana, M. Iliut, M. Turner, A. Vijayaraghavan, and I. Dierking, "Confinement effects on lyotropic nematic liquid crystal phases of graphene oxide dispersions," *2D Mater.*, vol. 4, no. 4, p. 041004, Aug. 2017, doi: 10.1088/2053-1583/aa843a.
[68] "Mechanism of Oxidization of Graphite to Graphene Oxide by the Hummers Method | ACS Omega." Accessed: Mar. 20, 2023. [Online]. Available: https://pubs.acs.org/doi/10.1021/acsomega.2c01963
[69] Y. A. Cheon, J. H. Bae, and B. G. Chung, "Reduced Graphene Oxide Nanosheet for Chemo-photothermal Therapy," *Langmuir*, vol. 32, no. 11, pp. 2731–2736, Mar. 2016, doi: 10.1021/acs.langmuir.6b00315.
[70] Y. Esmaeili, E. Bidram, A. Zarrabi, A. Amini, and C. Cheng, "Graphene oxide and its derivatives as promising In-vitro bio-imaging platforms," *Sci. Rep.*, vol. 10, no. 1, Art. no. 1, Oct. 2020, doi: 10.1038/s41598-020-75090-w.
[71] Y. Wu *et al.*, "Reduction of graphene oxide alters its cyto-compatibility towards primary and immortalized macrophages," *Nanoscale*, vol. 10, no. 30, pp. 14637–14650, Aug. 2018, doi: 10.1039/C8NR02798F.
[72] C. Tira, D. Tira, T. Simon, and S. Astilean, "Finite-Difference Time-Domain (FDTD) design of gold nanoparticle chains with specific surface plasmon resonance," *J. Mol. Struct.*, vol. 1072, pp. 137–143, Aug. 2014, doi: 10.1016/j.molstruc.2014.04.086.
[73] C. Xi, P. F. Marina, H. Xia, and D. Wang, "Directed self-assembly of gold nanoparticles into plasmonic chains," *Soft Matter*, vol. 11, no. 23, pp. 4562–4571, Jun. 2015, doi: 10.1039/C5SM00900F.
[74] V. Cucuiet *et al.*, "Gelatin-assisted fabrication of reduced nanographene oxide for dual-modal imaging of melanoma cells," *Colloids Surf. B Biointerfaces*, vol. 231, p. 113546, Nov. 2023, doi: 10.1016/j.colsurfb.2023.113546.
[75] A. C. Ferrari *et al.*, "Raman Spectrum of Graphene and Graphene Layers," *Phys. Rev. Lett.*, vol. 97, no. 18, p. 187401, Oct. 2006, doi: 10.1103/PhysRevLett.97.187401.
[76] I. Childres, L. Jauregui, W. Park, H. Cao, and Y. Chen, "Raman spectroscopy of graphene and related materials," *New Dev. Photon Mater. Res.*, vol. 1, 2013.
[77] A. Eckmann, "RAMAN SPECTROSCOPY OF GRAPHENE, ITS DERIVATIVES AND GRAPHENE-BASED HETEROSTRUCTURES," Doctorate Thesis, University of Manchester, Manchester, UK, 2013.
[78] J. Ambia-Garrido, A. Vainrub, and B. M. Pettitt, "A model for Structure and Thermodynamics of ssDNA and dsDNA Near a Surface: a Coarse Grained Approach," *Comput. Phys. Commun.*, vol. 181, no. 12, pp. 2001–2007, Dec. 2010, doi: 10.1016/j.cpc.2010.08.029.
[79] J. A. Dieringer *et al.*, "Introductory Lecture," *Faraday Discuss.*, vol. 132, no. 0, pp. 9–26, Apr. 2006, doi: 10.1039/B513431P.
[80] R. Yuge, M. Zhang, M. Tomonari, T. Yoshitake, S. Iijima, and M. Yudasaka, "Site Identification of Carboxyl Groups on Graphene Edges with Pt Derivatives," *ACS Nano*, vol. 2, no. 9, pp. 1865–1870, Sep. 2008, doi: 10.1021/nn800352y.

[81] D. Ayrat M., “Part I. Fundamentals. - Chapter 2. Mechanism of Formation and Chemical Structure of Graphene Oxide,” in *Graphene Oxide: Fundamentals and Applications*, Wiley, 2016, pp. 36–84.
[82] L. Anton, “Part I. Fundamentals - Chapter 1. Graphite Story - From the Beginning Till the Graphene Hype,” in *Graphene Oxide: Fundamentals and Applications*, Wiley, 2016, pp. 18–30.
[83] Y. Cui, Y. H. Lee, and J. W. Yang, “Impact of Carboxyl Groups in Graphene Oxide on Chemoselective Alcohol Oxidation with Ultra-Low Carbocatalyst Loading,” *Sci. Rep.*, vol. 7, no. 1, p. 3146, Jun. 2017, doi: 10.1038/s41598-017-03468-4.
[84] X. Liu, M. Atwater, J. Wang, and Q. Huo, “Extinction coefficient of gold nanoparticles with different sizes and different capping ligands,” *Colloids Surf. B Biointerfaces*, vol. 58, no. 1, pp. 3–7, Jul. 2007, doi: 10.1016/j.colsurfb.2006.08.005.

DECLARAȚIE PE PROPRIE RĂSPUNDERE

Subsemnatul, Cucuiet Vlad Gabriel, declar că Lucrarea de licență/diplomă/ **disertație** pe care o voi prezenta în cadrul examenului de finalizare a studiilor la Facultatea de Fizică din cadrul Universității Babeș-Bolyai, în sesiunea Iulie 2025, sub îndrumarea Conf. Dr. Monica Focșan reprezintă o operă personală. Menționez că nu am plagiat o altă lucrare publicată, prezentată public sau un fișier postat pe Internet. Pentru realizarea lucrării am folosit exclusiv bibliografia prezentată și nu am ascuns nici o altă sursă bibliografică sau fișier electronic pe care să le fi folosit la redactarea lucrării.

Prezenta declarație este parte a lucrării și se anexează la aceasta.

Data,

20.06.2025

Cucuiet Vlad-Gabriel